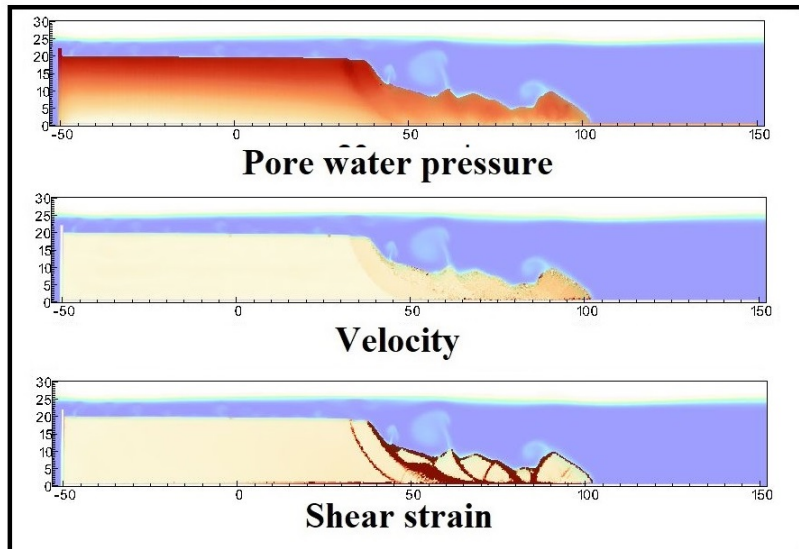


- 1 Graphical Abstract
- 2 MPMICE: A hybrid MPM-CFD model for simulating coupled problems in porous media. Application to earthquake-induced submarine landslides
- 3 Quoc Anh Tran, Gustav Grimstad, Seyed Ali Ghoreishian Amiri



**Application to earthquake-induced submarine landslide**

<sub>6</sub> Highlights

<sub>7</sub> **MPMICE: A hybrid MPM-CFD model for simulating coupled prob-**  
<sub>8</sub> **lems in porous media. Application to earthquake-induced subma-**  
<sub>9</sub> **rine landslides**

<sub>10</sub> Quoc Anh Tran, Gustav Grimstad, Seyed Ali Ghoreishian Amiri

- <sub>11</sub> • MPMICE is introduced for multiphase flow in porous media.
- <sub>12</sub> • Material Point method allows to model large deformation of non-isothermal
- <sub>13</sub> porous media.
- <sub>14</sub> • ICE (compressible multi-material CFD formulation) allows stabilizing
- <sub>15</sub> pore water pressure and turbulent flow.
- <sub>16</sub> • MPMICE is validated and apply to simulate the earthquake-induced
- <sub>17</sub> submarine landslide.

<sup>18</sup> MPMICE: A hybrid MPM-CFD model for simulating  
<sup>19</sup> coupled problems in porous media. Application to  
<sup>20</sup> earthquake-induced submarine landslides

<sup>21</sup> Quoc Anh Tran<sup>a</sup>, Gustav Grimstad<sup>a</sup>, Seyed Ali Ghoreishian Amiri<sup>a</sup>

<sup>a</sup>*Norwegian University of Science and Technology, , Trondheim, 7034, Norway*

---

## <sup>22</sup> Abstract

<sup>23</sup> In this paper, we describe a soil-fluid-structure interaction model that com-  
<sup>24</sup> bines soil mechanics (saturated sediments), fluid mechanics (seawater or air),  
<sup>25</sup> and solid mechanics (structures). The formulation combines the Material  
<sup>26</sup> Point Method, which models large deformation of the porous media and the  
<sup>27</sup> structure, with the Implicit Continuous-fluid Eulerian, which models com-  
<sup>28</sup> plex fluid flows. We validate the model and simulate the whole process of  
<sup>29</sup> earthquake-induced submarine landslides. We show that this model captures  
<sup>30</sup> complex interactions between saturated sediment, seawater, and structure,  
<sup>31</sup> so we can use the model to estimate the impact of potential submarine land-  
<sup>32</sup> slides on offshore structures.

<sup>33</sup> *Keywords:*

<sup>34</sup> Material Point Method, MPMICE, submarine landslide.

---

35	<b>Contents</b>	
36	<b>Nomenclature</b>	4
37	<b>Introduction</b>	6
38	<b>Theory and formulation</b>	8
39	Assumptions . . . . .	8
40	Governing equations . . . . .	9
41	Constitutive soil model . . . . .	11
42	Turbulent model . . . . .	12
43	Frictional force for soil-structure interaction . . . . .	12
44	Momentum and Energy exchange model . . . . .	13
45	Solving momentum and energy exchange with an implicit solver	14
46	Equation of state for fluid phases . . . . .	16
47	<b>Numerical implementation</b>	17
48	Interpolation from Solid Particle to Grid . . . . .	18
49	Compute equation of state for fluid phase . . . . .	20
50	Compute cell face velocity . . . . .	20
51	Compute cell face temperature . . . . .	21
52	Compute fluid pressure (implicit scheme) . . . . .	22
53	Compute viscous shear stress term of the fluid phase . . . . .	22
54	Compute nodal internal temperature of the solid phase . . . . .	22
55	Compute and integrate acceleration of the solid phase . . . . .	23
56	Compute Lagrangian value (mass, momentum and energy) . . . . .	23
57	Compute Lagrangian specific volume of the fluid phase . . . . .	24
58	Compute advection term and advance in time . . . . .	25
59	Interpolate from cell to node of the solid phase . . . . .	26
60	Update the particle variables . . . . .	26
61	<b>Numerical examples</b>	27
62	Fluid Flow through isothermal porous media . . . . .	27
63	Isothermal consolidation . . . . .	28
64	Thermal induced cavity flow . . . . .	29
65	Underwater debris flow . . . . .	30
66	Validation of soil response to the seismic loading . . . . .	34
67	Earthquake-induced submarine landslides . . . . .	36

68	<b>Conclusions</b>	41
69	<b>Acknowledgements</b>	42
70	<b>Appendix: Equation derivation</b>	42
71	Evolution of porosity . . . . .	42
72	Momentum conservation . . . . .	43
73	Energy conservation . . . . .	44
74	Advanced Fluid Pressure . . . . .	45
75	Momentum and Energy exchange with an implicit solver . . . . .	46

<sup>76</sup> **Nomenclature**

**General variables**

<u>Variable</u>	<u>Dimensions</u>	<u>Description</u>
$V$	$[L^3]$	Representative volume
$n$		Porosity
$\sigma$	$[ML^{-1}t^{-2}]$	Total stress tensor
$\Delta t$	$[t]$	Time increment
$\mathbf{b}$	$[ML^1t^{-2}]$	Body force
$c_v$	$[L^2t^{-2}T^{-1}]$	Constant volume specific heat
$f_d$	$[MLt^{-2}]$	Drag forces in momentum exchange term
$f^{int}$	$[MLt^{-2}]$	Internal forces
$f^{ext}$	$[MLt^{-2}]$	External forces
$q_{fs}$	$[MLt^{-2}]$	Heat exchange term
$S$		Weighting function
$\nabla S$		Gradient of weighting function

<sup>77</sup>

**Solid phase**

<u>Variable</u>	<u>Dimensions</u>	<u>Description</u>
$m_s$	$[M]$	Solid mass
$\rho_s$	$[ML^{-3}]$	Solid density
$\phi_s$		Solid volume fraction
$\bar{\rho}_s$	$[ML^{-3}]$	Bulk Solid density
$\mathbf{x}_s$	$[L]$	Solid Position vector
$\mathbf{U}_s$	$[Lt^{-1}]$	Solid Velocity vector
$\mathbf{a}_s$	$[Lt^{-2}]$	Solid Acceleration vector
$\sigma'$	$[ML^{-1}t^{-2}]$	Effective Stress tensor
$\epsilon_s$		Strain tensor
$e_s$	$[L^2t^{-2}]$	Solid Internal energy per unit mass
$T_s$	$[T]$	Solid Temperature
$\mathbf{F}_s$		Solid Deformation gradient
$V_s$	$[L^3]$	Solid Volume

**Fluid phase**

<u>Variable</u>	<u>Dimensions</u>	<u>Description</u>
$m_f$	[M]	Fluid mass
$\rho_f$	[ML <sup>-3</sup> ]	Fluid density
$\phi_f$		Fluid volume fraction
$\bar{\rho}_f$	[ML <sup>-3</sup> ]	Bulk Fluid density
$\mathbf{U}_f$	[Lt <sup>-1</sup> ]	Fluid Velocity vector
$\boldsymbol{\sigma}_f$	[ML <sup>-1</sup> t <sup>-2</sup> ]	Fluid stress tensor
$p_f$	[ML <sup>-1</sup> t <sup>-2</sup> ]	Fluid isotropic pressure
$\boldsymbol{\tau}_f$	[ML <sup>-1</sup> t <sup>-2</sup> ]	Fluid shear stress tensor
$e_f$	[L <sup>2</sup> t <sup>-2</sup> ]	Fluid Internal energy per unit mass
$T_f$	[T]	Fluid Temperature
$v_f$	[L <sup>3</sup> /M]	Fluid Specific volume $\frac{1}{\rho_f}$
$\alpha_f$	[1/T]	Thermal expansion
$\mu$	[ML <sup>-1</sup> t <sup>-1</sup> ]	Fluid viscosity
$V_f$	[L <sup>3</sup> ]	Fluid Volume

**Superscript**

<u>Variable</u>	<u>Dimensions</u>	<u>Description</u>
$n$		Current time step
$L$		Lagrangian values
$n + 1$		Next time step

**Subscript**

$c$	Cell-centered quantity
$p$	Particle quantity
$i$	Node quantity
$FC$	Cell face quantity
$L, R$	Left and Right cell faces

79 **Introduction**

80 Many geological natural processes and their interactions with man-made  
81 structures are influenced by soil-fluid-structure interactions. The prediction  
82 of these processes requires a tool that can capture complex interactions  
83 between soil, fluid, and structure, such as the process of submarine land-  
84 slides. Indeed, The offshore infrastructure as well as coastal communities  
85 may be vulnerable to submarine landslides. Submarine landslides contain  
86 three stages: triggering, failure, and post-failure. Erosion or earthquakes can  
87 trigger slope failures in the first stage. Following the failure, sediments move  
88 quickly after the post-failure stage. In other words, solid-like sediments will  
89 behave like a fluid after failure. This phase transition makes the simulation  
90 of submarine landslides a challenging task.

91  
92 Due to this phase transition, submarine landslide can be modeled by ei-  
93 ther the Computational Fluid Dynamics (CFD) or the particle-based meth-  
94 ods. For simulating submarine slides, CFD methods solve governing equa-  
95 tions in a full-Eulerian framework [1, 2, 3, 4] with interface capturing tech-  
96 niques. While CFD can handle complex flows (such as turbulent flows), it  
97 cannot account for the triggering mechanism of submarine landslides because  
98 it is not straightforward to consider 'soil constitutive laws' of sediment ma-  
99 terials in the Eulerian framework. In contrast, particle-based methods can  
100 overcome this problem by using the Lagrangian framework. These meth-  
101 ods have been extensively used to simulate landslides, like Material Point  
102 Method (MPM) [5], Smooth Particle Hydro Dynamics [6], Particle Finite  
103 Element Method [7], or Coupled Eulerian Lagrangian Method [8]. For sim-  
104 plicity, these simulations adopt total stress analysis which neglects the pore  
105 pressure development which is key factor triggering slope failures.

106  
107 Recent developments in particle-based methods model the coupling of  
108 fluid flows in porous media by sets of Lagrangian particles. For the MPM  
109 family, it is the double-point MPM ([9, 10, 11]) where fluid particles and  
110 solid particles are overlapped in a single computational grid. Even if fluid  
111 flows are considered, particle-based methods have numerical instability in  
112 modeling the fluid flow, which requires additional numerical treatments such  
113 as the B-bar method [9], null-space filter [12], or least square approximation  
114 [13, 14]. Indeed, CFD is a more optimal option for complex fluid flows  
115 especially dealing with large distortions of continuum fluid media. Therefore,

116 it could be ideal to combine the CFD with particle-based methods. More than  
 117 50 particle-based methods have been developed to solve large deformations  
 118 of solids over the last two decades [15], but the MPM appears to be the  
 119 best candidate for coupling with the CFD. Because MPM incorporates a  
 120 stationary mesh during computation, just like CFD. As such, both MPM  
 121 and CFD can be coupled naturally in a unified computational mesh.



*Figure 1: Interaction between soil-fluid-structure*

122

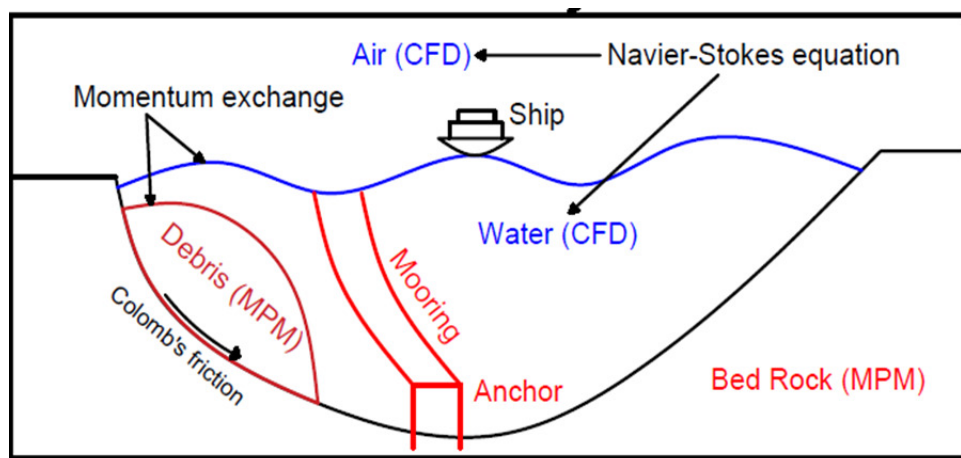


*Figure 2: Coupling of soil-water-structure interaction using MPMICE*

123 A numerical method for simulating soil-fluid-structure interaction (Figure  
124 1) involving large deformations, is presented in this work in order to simu-  
125 late the interaction between sediment (soil), seawater (fluid) and offshore  
126 structures (structure) namely MPMICE (Figure 2). In the MPMICE, the  
127 Material Point Method (MPM) is coupled with the Implicit Continuous Eu-  
128 lerian (ICE). The MPM method is a particle method that allows the porous  
129 soil to undergo arbitrary distortions. The ICE method, on the other hand,  
130 is a conservative finite volume technique with all state variables located at  
131 the cell center (temperature, velocity, mass, pressure). An initial technical  
132 report [16] at Los Alamos National Laboratory provided the theoretical and  
133 algorithmic foundation for the MPMICE, followed by the MPMICE devel-  
134 opment and implementation in the high-performance Uintah computational  
135 framework for simulating fluid-structure interactions [17]. This paper pri-  
136 marily contributes further to the development of the MPMICE for analyzing  
137 the **soil**-fluid-structure interaction, since sediment should be considered as a  
138 porous media (soil) and not as a solid to capture the evolution of the pore  
139 water pressure. Baumgarten et al. [18] made the first attempt at coupling  
140 the Finite Volume Method with the MPM for the simulation of soil-fluid  
141 interaction. In contrast to the mentioned work, we use implicit time inte-  
142 gration for the multi phase flows instead of explicit time integration for the  
143 single-phase flow.

#### 144 **Theory and formulation**

145 This section lay out the theoretical framework for the MPMICE model.  
146 We use the common notation of the continuum mechanics with vector and  
147 tensor denoted simply by using bold font and scalar denoted by using normal  
148 font. The notation are shown in Nomenclature.

#### 149 *Assumptions*

150 The following assumptions are made for the MPMICE model.

- 151 1. Solid phases (MPM) are described in a Lagrangian formulation while  
152 fluid phases (ICE) are described in an Eulerian formulation in the  
153 framework of continuum mechanics and mixture theory.
- 154 2. Solid grains are incompressible while the fluid phases are compressible.  
155 Solid's thermal expansion is negligible.
- 156 3. There is no mass exchange between solid and fluid phases.
- 157 4. Terzaghi's effective stress is valid.

158 *Governing equations*

159 A representative element volume  $\Omega$  is decomposed by two domains: solid  
160 domains  $\Omega_s$  and fluid domains  $\Omega_f$ . Then, all domains are homogenized  
161 into two overlapping continua. Considering the volume fraction of solid  
162  $\phi_s = \Omega_s/\Omega$  and fluid  $\phi_f = \Omega_f/\Omega$  with the true (or Eulerian) porosity  
163  $n = \sum \phi_f$  of the representative element volume, the average density of solid  
164 and fluid phases are defined as:

165

$$\bar{\rho}_s = \phi_s \rho_s, \quad \bar{\rho}_f = \phi_f \rho_f \quad (1)$$

166 The mass of solid and fluid phases are:

167

$$m_s = \int_{\Omega_s} \rho_s dV = \bar{\rho}_s V, \quad m_f = \int_{\Omega_f} \rho_f dV = \bar{\rho}_f V \quad (2)$$

168 Reviewing the Terzaghi's effective stress concept for the saturated porous  
169 media, the total stress  $\boldsymbol{\sigma}$  is calculated by:

170

$$\boldsymbol{\sigma} = \boldsymbol{\sigma}' - p_f \mathbf{I} \quad (3)$$

171 The balance equations are derived based on the mixture theory. The rep-  
172 resentative thermodynamic state of the fluid phases are given by the vector  
173  $[m_f, \mathbf{U}_f, e_f, T_f, v_f]$  which are mass, velocity, internal energy, temperature,  
174 specific volume. The representative state of the solid phases are given by the  
175 vector  $[m_s, \mathbf{U}_s, e_s, T_s, \boldsymbol{\sigma}', p_f]$  which are mass, velocity, internal energy, temper-  
176 ature, effective stress and pore water pressure. The derivation is presented  
177 in detail in the Appendix.

178

---

179 Mass Conservation

180 The mass balance equations for both fluid (e.g., water, air) and solid phases  
181 are:

182

$$\frac{1}{V} \frac{\partial m_f}{\partial t} + \nabla \cdot (m_f \mathbf{U}_f) = 0, \quad \frac{1}{V} \frac{D_s m_s}{Dt} = 0 \quad (4)$$

183 Solving the mass balance equation leads to:

$$\frac{D_s n}{Dt} = \phi_s \nabla \cdot \mathbf{U}_s \quad (5)$$

184

---

185 Momentum Conservation

<sub>186</sub> The momentum balance equations for the fluid phases (e.g., water, air) are:

$$\frac{1}{V} \left[ \frac{\partial(m_f \mathbf{U}_f)}{\partial t} + \nabla \cdot (m_f \mathbf{U}_f \mathbf{U}_f) \right] = -\phi_f \nabla p_f + \nabla \cdot \boldsymbol{\tau}_f + \bar{\rho}_f \mathbf{b} + \sum \mathbf{f}_d \quad (6)$$

<sub>187</sub> The momentum balance equations for the solid phases are:

$$\frac{1}{V} \frac{D_s(m_s \mathbf{U}_s)}{Dt} = \nabla \cdot (\boldsymbol{\sigma}') - \phi_s \nabla p_f + \bar{\rho}_s \mathbf{b} + \sum \mathbf{f}_{fric} - \sum \mathbf{f}_d \quad (7)$$

<sub>188</sub>

---

### <sub>189</sub> Energy Conservation

<sub>190</sub> The internal energy balance equations for the fluid phases (e.g., water, air)  
<sub>191</sub> are:

$$\frac{1}{V} \left[ \frac{\partial(m_f e_f)}{\partial t} + \nabla \cdot (m_f e_f \mathbf{U}_f) \right] = -\bar{\rho}_f p_f \frac{D_f v_f}{Dt} + \boldsymbol{\tau}_f : \nabla \mathbf{U}_f + \nabla \cdot \mathbf{q}_f + \sum q_{sf} \quad (8)$$

<sub>192</sub> The internal energy balance equations for the solid phase are:

$$\frac{m_s}{V} c_v \frac{D_s(T_s)}{Dt} = \boldsymbol{\sigma}' : \frac{D_s(\boldsymbol{\epsilon}_s^p)}{Dt} + \nabla \cdot \mathbf{q}_s - \sum q_{sf} \quad (9)$$

<sub>193</sub> where  $c_v$  is the specific heat at constant volume of the solid materials.

<sub>194</sub>

---

<sub>195</sub> Closing the systems of equations, the following additional models are needed:

<sub>196</sub> (1) A constitutive equation to describe the stress - strain behaviour of solid  
<sub>197</sub> phase (computing effective stress  $\boldsymbol{\sigma}'$ ).

<sub>198</sub> (2) Optional turbulent model to compute the viscous shear stress  $\boldsymbol{\tau}_f$ .

<sub>199</sub> (3) Frictional forces  $\mathbf{f}_{fric}$  for the contact for soil-structure interaction be-  
<sub>200</sub> tween solid/porous materials with the friction coefficient  $\mu_{fric}$ .

<sub>201</sub> (4) Exchange momentum models (computing drag force  $\mathbf{f}_d$ ) for interaction  
<sub>202</sub> between materials.

<sub>203</sub> (5) Energy exchange models (computing temerature exhangre term  $q_{sf}$ ) for  
<sub>204</sub> interaction between materials.

<sub>205</sub> (6) An equation of state to establish relations between thermodynamics vari-  
<sub>206</sub> ables of each fluid materials  $[P_f, \bar{\rho}_f, v_f, T_f, e_f]$ .

<sup>207</sup> Four thermodynamic relations for the equation of states are:

$$\begin{aligned} e_f &= e_f(T_f, v_f) \\ P_f &= P_f(T_f, v_f) \\ \phi_f &= v_f \bar{\rho}_f \\ 0 &= n - \sum_{f=1}^{N_f} v_f \bar{\rho}_f \end{aligned} \quad (10)$$

<sup>208</sup> *Constitutive soil model*

<sup>209</sup> As a result of the explicit MPM formulation, we can derive the consti-  
<sup>210</sup> tutive law in the updated Lagrangian framework of "small strain - large  
<sup>211</sup> deformation". Therefore, the rotation of the particles (representative ele-  
<sup>212</sup> ment volume) is manipulated by rotating the Cauchy stress tensor. First,  
<sup>213</sup> the deformation gradient is decomposed into the polar rotation tensor  $\mathbf{R}_s^{n+1}$   
<sup>214</sup> and stretch tensor  $\mathbf{V}_s^{n+1}$  as:

$$\mathbf{F}_s^{n+1} = \mathbf{V}_s^{n+1} \mathbf{R}_s^{n+1} \quad (11)$$

<sup>215</sup> Then, before calling the constitutive model, the stress and strain rate tensor  
<sup>216</sup> are rotated to the reference configuration as:

$$\boldsymbol{\sigma}'^{n*} = (\mathbf{R}_s^{n+1})^T \boldsymbol{\sigma}'^{n*} \mathbf{R}_s^{n+1} \quad (12)$$

$$\delta\boldsymbol{\epsilon}^{n*} = (\mathbf{R}_s^{n+1})^T \delta\boldsymbol{\epsilon}_s^{n*} \mathbf{R}_s^{n+1} \quad (13)$$

<sup>218</sup> Using the constitutive model with the input tensors  $\boldsymbol{\sigma}'^{n*}, \delta\boldsymbol{\epsilon}^{n*}$  to compute  
<sup>219</sup> the Cauchy stress tensor at the advanced time step  $\boldsymbol{\sigma}'^{n+1*}$  then rotating it  
<sup>220</sup> back to current configuration as:

$$\boldsymbol{\sigma}'^{n+1} = \mathbf{R}_s^{n+1} \boldsymbol{\sigma}'^{n+1*} (\mathbf{R}_s^{n+1})^T \quad (14)$$

<sup>221</sup> In this paper, we adopt the hyper-elastic Neo Hookean model for the structure  
<sup>222</sup> materials and additionally Mohr-Coulomb failure criteria for the soil (porous  
<sup>223</sup> media) materials. The Cauchy stress of the hyper-elastic Neo Hookean model  
<sup>224</sup> can be written as:

$$\boldsymbol{\sigma}' = \frac{\lambda \ln(J)}{J} + \frac{\mu}{J} (\mathbf{F} \mathbf{F}^T - \mathbf{J}) \quad (15)$$

<sup>225</sup> where  $\lambda$  and  $\mu$  are bulk and shear modulus ad  $J$  is the determinant of the  
<sup>226</sup> deformation gradient  $\mathbf{F}$ . And the yield function  $f$  and flow potentials  $g$  of

<sup>227</sup> the Mohr-Coulomb can be written as:

$$\begin{aligned} f &= \sigma'_1 - \sigma'_3 - 2c' \cos(\phi') - (\sigma'_1 + \sigma'_3) \sin(\phi') \\ g &= \sigma'_1 - \sigma'_3 - 2c' \cos(\psi') - (\sigma'_1 + \sigma'_3) \sin(\psi') \end{aligned} \quad (16)$$

<sup>228</sup> where the  $c'$ ,  $\phi'$  and  $\psi'$  are cohesion and friction angle and dilation angle.  $\sigma'_1$   
<sup>229</sup> and  $\sigma'_3$  are maximum and minimum principal stress.

<sup>230</sup> *Turbulent model*

<sup>231</sup> The turbulent effect is modelled using a statistical approach namely large-  
<sup>232</sup> eddy simulation. In this approach, the micro-scale turbulent influence in the  
<sup>233</sup> dynamics of the macro-scale motion is computed through simple models like  
<sup>234</sup> Smagorinsky model. In the Smagorinsky model, the residual stress tensor is:

$$\tau_{ij} = 2\mu_{eff}(\bar{S}_{ij} - \frac{1}{3}\delta_{ij}\bar{S}_{kk}) + \frac{1}{3}\delta_{ij}\tau_{kk} \quad (17)$$

<sup>235</sup> where the strain rate tensor is given by:

$$\bar{S}_{ij} = \frac{1}{2}(\frac{\delta \bar{U}_i}{\delta x_j} + \frac{\delta \bar{U}_j}{\delta x_i}) \quad (18)$$

<sup>236</sup> and the effective viscosity is sum of molecular viscosity and turbulent viscosity  
<sup>237</sup>  $\mu_{eff} = \mu + \mu_t$  in which the turbulent viscosity  $\mu_t$  is calculated by:

$$\mu_t = (C_s \Delta)^2 \sqrt{2\bar{S}_{ij}\bar{S}_{ij}} \quad (19)$$

<sup>238</sup> where  $C_s$  is the Smagorinsky constant with the value of 0.1 and  $\Delta = \sqrt[3]{dxdydz}$   
<sup>239</sup> is the grid size that defines the subgrid length scale.

<sup>240</sup> *Frictional force for soil-structure interaction*

<sup>241</sup> MPMICE includes a contact law for the interaction between soil and  
<sup>242</sup> structure using the first Coulomb friction contact for MPM presented by  
<sup>243</sup> Bardenhagen et al. ([19]). The magnitude of the friction force at the contact  
<sup>244</sup> depends on the friction coefficient  $\mu_{fric}$  and the normal force  $\mathbf{f}_{norm}$  computed  
<sup>245</sup> from the projection of the contact force in the normal direction.

$$\mathbf{f}_{fric} = \mu_{fric} \mathbf{f}_{norm} \quad (20)$$

246 The contact determines whether the soil is sliding or sticking to the structure  
 247 by comparing the friction force with the sticking force  $\mathbf{f}_{stick}$  computed from  
 248 the projection of the contact force in the tangent direction as:

$$\begin{aligned} \text{if } \mathbf{f}_{fric} \geq \mathbf{f}_{stick} & \text{ no sliding} \\ \text{if } \mathbf{f}_{fric} < \mathbf{f}_{stick} & \text{ sliding occurs} \end{aligned} \quad (21)$$

249 Frictional sliding between solid materials also generates dissipation and the  
 250 work rate generated from the sliding can be calculated as:

$$\Delta W_{friction} = \mathbf{f}_{fric} d \quad (22)$$

251 where  $d$  is the sliding distance which can be computed based on the sliding  
 252 velocity between two materials.

253 *Momentum and Energy exchange model*

254 Currently, the energy exchange coefficient  $H_{sf}$  is assumed to be constant  
 255 for the sake of simplicity. Then the energy exchange can be written as:

$$q_{sf} = H_{sf}(T_f - T_s) \quad (23)$$

256 On the other hand, the drag force can be calculated as:

$$f_d = K(\mathbf{U}_s - \mathbf{U}_f) \quad (24)$$

257 For the momentum exchange between fluid flows and porous media, we as-  
 258 sume that the drag force  $\mathbf{f}_d$  depends on the average grain size of the grains  
 259  $D_p$ , the porosity  $n$ , the fluid viscosity  $\mu_f$ , and is proportional to the relative  
 260 velocities of soil grains and fluid  $(\mathbf{U}_s - \mathbf{U}_f)$ . Based on recent investigation  
 261 of CFD simulations of fluid flow around mono- and bi-disperse packing of  
 262 spheres for  $0.1 < \phi_s < 0.6$  and  $Re < 1000$  [20]. The drag force is given by:

$$\mathbf{f}_d = \frac{18\phi_s(1-\phi_s)\mu_f}{D_p^2} F(\phi_s, Re)(\mathbf{U}_s - \mathbf{U}_f) \quad (25)$$

263 where Reynolds number  $Re$  are computed as:

$$Re = \frac{n\rho_f D_p}{\mu_f} \|(\mathbf{U}_s - \mathbf{U}_f)\| \quad (26)$$

<sup>265</sup> The function  $F(\phi_s, Re)$  can be calculated as:

$$F(\phi_s, Re) = F(\phi_s, 0) + \frac{0.413Re}{24(1 - \phi_s)^2} \left( \frac{(1 - \phi_s)^{-1} + 3\phi_s(1 - \phi_s) + 8.4Re^{-0.343}}{1 + 10^{3\phi_s}Re^{-(1+4\phi_s)/2}} \right) \quad (27)$$

<sup>266</sup> where the low Reynold coefficient  $F(\phi_s, Re \rightarrow 0)$  is:

$$F(\phi_s, 0) = \frac{10\phi_s}{(1 - \phi_s)^2} + (1 - \phi_s)^2(1 + 1.5\sqrt{\phi_s}) \quad (28)$$

<sup>267</sup> When validating the model with analytical solution, it requires to know the  
<sup>268</sup> hydraulic conductivity  $K$ . In such case, we convert the equation (29) to  
<sup>269</sup> Kozeny-Carman formula by assuming  $F(\phi_s, Re) = 10\phi_s/(1 - \phi_s)^2$ , leading to

$$\mathbf{f}_d = \frac{180\phi_s^2\mu_f}{D_p^2(1 - \phi_s)} (\mathbf{U}_s - \mathbf{U}_f) \quad (29)$$

<sup>270</sup> Then, the draging force following the Darcy law is given by:

$$\mathbf{f}_d = \frac{n^2\mu_f}{\kappa} (\mathbf{U}_s - \mathbf{U}_f) \quad (30)$$

<sup>271</sup> where  $\kappa$  being intrinsic permeability of soil which can be written as:

$$\kappa = \frac{K\mu_f}{\rho_f g} \quad (31)$$

<sup>272</sup> As such, the hydraulic conductivity will be expressed as:

$$K = \frac{D_p^2(1 - \phi_s)^3}{180\phi_s^2\mu_f} \rho_f g \quad (32)$$

<sup>273</sup> *Solving momentum and energy exchange with an implicit solver*

<sup>274</sup> The derivation of the implicit integration for the momentum exchange is  
<sup>275</sup> presented in the Appendix's section 'Momentum and energy exchange with  
<sup>276</sup> an implicit solver'. The linear equations for multi phases i,j=1:N has the  
<sup>277</sup> form as:

$$\begin{vmatrix} (1 + \beta_{ij}) & -\beta_{ij} \\ -\beta_{ji} & (1 + \beta_{ji}) \end{vmatrix} \begin{vmatrix} \Delta\mathbf{U}_i \\ \Delta\mathbf{U}_j \end{vmatrix} = \begin{vmatrix} \beta_{ij}(\mathbf{U}_i^* - \mathbf{U}_j^*) \\ \beta_{ji}(\mathbf{U}_i^* - \mathbf{U}_j^*) \end{vmatrix}$$

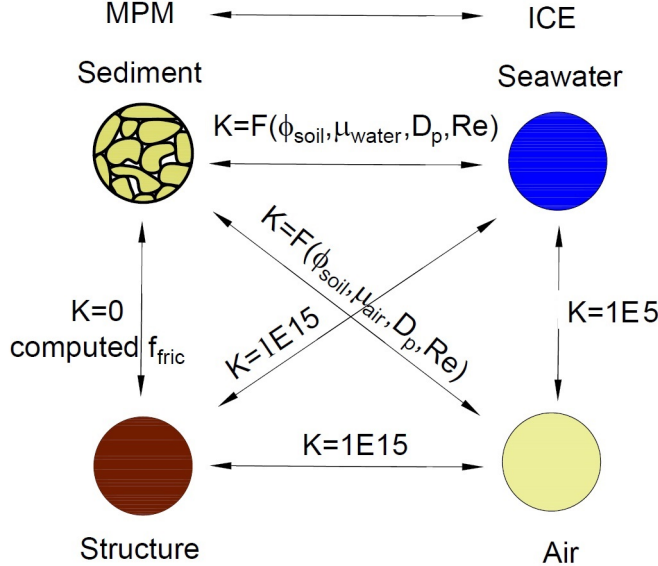


Figure 3: Momentum exchange coefficient between materials

278 where the intermediate velocity for fluid phases  $f=1:N_f$  and for solid/porous  
279 phases  $s=1:N_s$  can be calculated by:

$$\begin{aligned} U_f^* &= U_f^n + \Delta t \left( -\frac{\nabla P_f^{n+1}}{\rho_f^n} + \frac{\nabla \cdot \tau_f^n}{\bar{\rho}_f^n} + \mathbf{b} \right) \\ U_s^* &= U_s^n + \Delta t \left( \frac{\nabla \cdot \sigma'^n}{\bar{\rho}_s^n} - \frac{\nabla P_f^{n+1}}{\rho_s} + \mathbf{b} \right) \end{aligned} \quad (33)$$

280 Also, the momentum exchange coefficient can be computed at every time  
281 step as  $\beta_{12} = K/\bar{\rho}_f^n$  and  $\beta_{21} = K/\bar{\rho}_s^n$  with the coefficient depending on the  
282 different type of interactions (see Figure 3) as for example:

283

- 284 1. The drag force is set to zero in soil-structure interactions, and instead  
285 the frictional force is computed.
- 286 2. As a result of fluid-structure interaction, the momentum exchange coef-  
287 ficient should be extremely high (1E15) when the solid material points  
288 are considered to be zero-porosity/zero-permeability.
- 289 3. In the case of soil-fluid interaction, the drag force is calculated using  
290 the equation (29). Considering that air has a much lower viscosity than

water, its drag force is much lower than the drag force of water in a pore.

4. A momentum exchange coefficient of 1E5 is applied between multiphase flows. This value is far higher than reality [21], but it is necessary to have enough numerical stability to conduct simulations in the numerical example.

Similar approach applied for the energy exchange term leading to:

$$\begin{vmatrix} (1 + \eta_{ij}) & -\eta_{ij} \\ -\eta_{ji} & (1 + \eta_{ji}) \end{vmatrix} \begin{vmatrix} \Delta T_i \\ \Delta T_j \end{vmatrix} = \begin{vmatrix} \eta_{ij}(T_i^n - T_j^n) \\ \eta_{ji}(T_j^n - T_i^n) \end{vmatrix}$$

with  $\eta$  being the energy exchange coefficient.

*Equation of state for fluid phases*

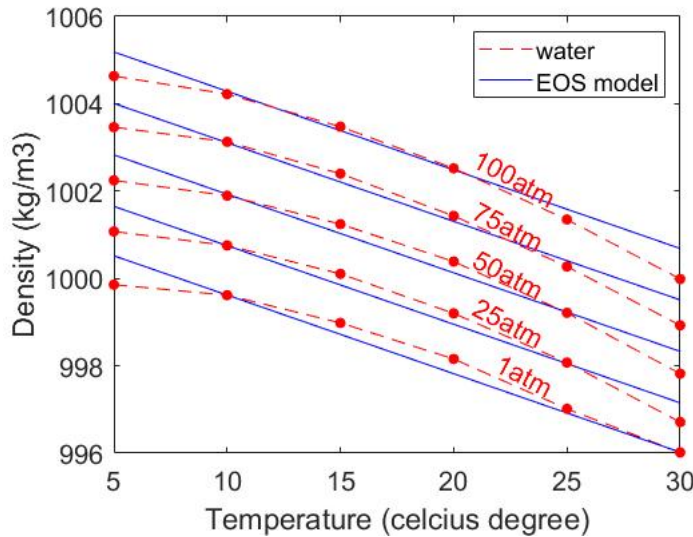


Figure 4: Equation of state of water

The equation of state establishes relations between thermodynamics variables  $[P_f, \rho_f, T_f]$ . The choice of the equation of state depends on the types of the fluid materials. For example, for the air, it is possible to assume the equation of state for the perfect gas which obeys:

$$P_f = \rho_f R T_f \quad (34)$$

304 where  $R$  is the gas constant. For the water, a simple linear equation of state  
 305 is in the following form:

$$P_f = P_{ref} + K_f(\rho_f - \rho_{ref} - \alpha_f(T_f - T_{ref})) \quad (35)$$

306 where reference pressure  $P_{ref} = 1$  atm = 101325 Pa, reference temperature  
 307  $T_{ref} = 10^\circ\text{C}$ , reference density  $\rho_{ref} = 999.8 \text{ kg/m}^3$ , the bulk modulus of water  
 308  $K_f = 2 \text{ GPa}$ , and the water thermal expansion  $\alpha_f = 0.18 \text{ }^\circ\text{C}^{-1}$ . Equation  
 309 (35) matches well with the state of the water (see Figure 4).

310 **Numerical implementation**

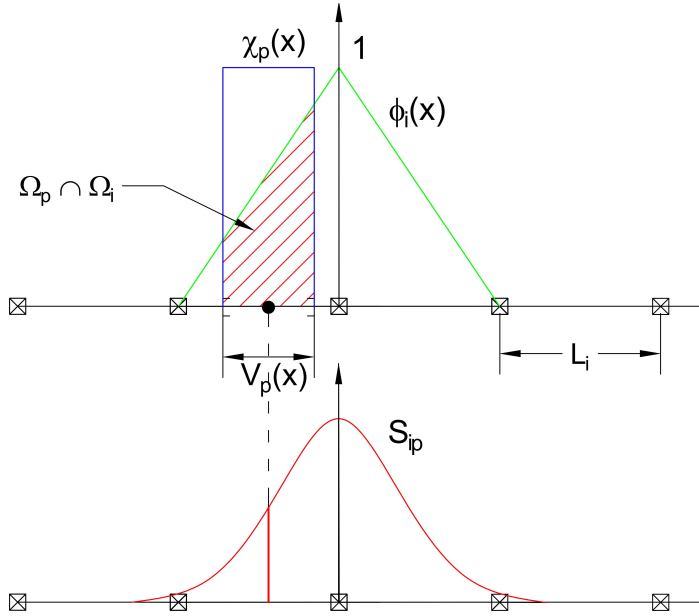


Figure 5: GIMP weighting function (red as a convolution of the linear basis shape function (green) and the characteristic function (blue)

311 The fluid phases are discretized in the grid with the state variables stored  
 312 at the centroid of the cells  $[\rho_{f,c}, \mathbf{U}_{f,c}, T_{f,c}, v_{f,c}]$  while the solid phase is dis-  
 313 cretized in the particles with the state variables  $[m_{sp}, \mathbf{U}_{sp}, T_{sp}, \boldsymbol{\sigma}'_{sp}]$ . In the  
 314 Material Point Method, we use the generalized interpolation technique [22]  
 315 using the weight function as a convolution of a grid shape function  $N_i(\mathbf{x})$  in

<sup>316</sup> a nodal domain  $\Omega_i$  and a characteristic function  $\chi_p(\mathbf{x})$  in a particle domain  
<sup>317</sup>  $\Omega_p$  with the volume  $V_p(\mathbf{x})$  as follows:

$$S_{ip} = \frac{1}{V_p} \int_{\Omega_i \cap \Omega_p} N_i(\mathbf{x}) \chi_p(\mathbf{x}) d\mathbf{x} \quad (36)$$

<sup>318</sup> where the volume  $V_p(\mathbf{x})$  of the material point p can be calculated as:

$$V_p = \int_{\Omega_p} \chi_p(\mathbf{x}) d\mathbf{x} \quad (37)$$

<sup>319</sup> The characteristic function is the Heaviside function as  $\chi_p = 1$  if  $\mathbf{x} \in \Omega_p$ ,  
<sup>320</sup> otherwise 0 (see Figure 5). For the interpolation of the centroid of the cell,  
<sup>321</sup> the linear basis function is used as:

$$S_{ci} = N_i(\mathbf{x}_c) \quad (38)$$

<sup>322</sup> The time discretization are solved using the following steps.

### <sup>323</sup> *Interpolation from Solid Particle to Grid*

<sup>324</sup> The nodal values of the solid state (mass, velocity, temperature, volume)  
<sup>325</sup> are:

$$\begin{aligned} m_{si}^n &= \sum S_{ip} m_{sp} \\ \mathbf{U}_{si}^n &= \frac{\sum S_{ip} (m\mathbf{U})_{sp}^n}{m_{si}^n} \\ T_{si}^n &= \frac{\sum S_{ip} (mT)_{sp}^n}{m_{si}^n} \\ V_{si}^n &= \frac{\sum S_{ip} (mV)_{sp}^n}{m_{si}^n} \\ \boldsymbol{\sigma}_{si}^n &= \frac{\sum S_{ip} (\boldsymbol{\sigma}V)_{sp}^n}{V_{si}^n} \end{aligned} \quad (39)$$

<sup>326</sup> The nodal internal forces is calculated by:

$$\mathbf{f}_{si}^{int,n} = - \sum \nabla S_{ip} (\boldsymbol{\sigma}'_{sp})^n V_{sp}^n \quad (40)$$

<sup>327</sup> The nodal external forces  $f_{si}^{ext,n}$  and the nodal frictional forces  $f_{si}^{fric}$  from  
<sup>328</sup> contact between materials are computed here.

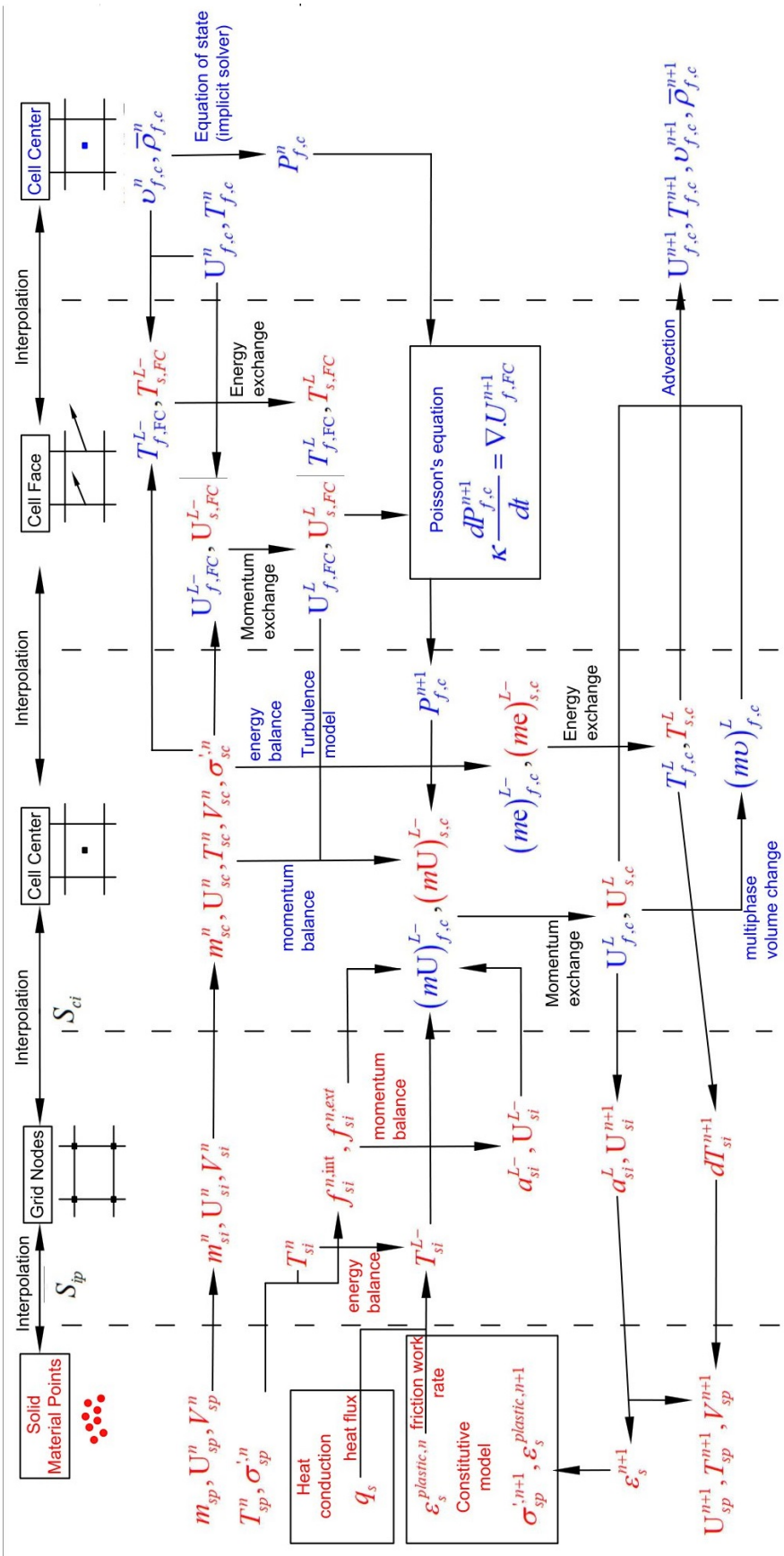


Figure 6: Numerical implementation of MP-MICE

<sup>329</sup> Then we compute the solid cell variables as:

$$\begin{aligned}
 m_{sc}^n &= \sum S_{ci} m_{si} \\
 \rho_{sc}^n &= \frac{m_{sc}^n}{V} \\
 \mathbf{U}_{sc}^n &= \sum S_{ci} \mathbf{U}_{si}^n \\
 T_{sc}^n &= \sum S_{ci} T_{si}^n \\
 V_{sc}^n &= \sum S_{ci} V_{si}^n \\
 \boldsymbol{\sigma}_{sc}^n &= \sum S_{ci} \boldsymbol{\sigma}_{si}^n
 \end{aligned} \tag{41}$$

<sup>330</sup> *Compute equation of state for fluid phase*

<sup>331</sup> The total fluid material volume of a cell is:

$$V_{total} = \sum_{f=1}^{N_f} M_f v_f \tag{42}$$

<sup>332</sup> We need to find  $P_{f,c}^n$  which allows each fluid materials obey their equation of  
<sup>333</sup> states  $[P_f, \rho_f, v_f, T_f, e_f]$  but also allow mass of all fluid materials to fill the  
<sup>334</sup> entire the pore volume without ongoing compression or expansion following  
<sup>335</sup> the condition as follows:

$$0 = n - \sum_{f=1}^{N_f} v_f \bar{\rho}_f \tag{43}$$

<sup>336</sup> Then, we can use the Newton-Raphson interation to find the value of  $P_{f,c}^n$   
<sup>337</sup> which satisfies the equation (42, 43) and each equation of states of each fluid  
<sup>338</sup> materials.

<sup>339</sup> *Compute cell face velocity*

<sup>340</sup> Following the derivation in the Appendix: Advanced Fluid Pressure, we  
<sup>341</sup> first compute the fluid cell face velocity as:

$$\mathbf{U}_{f,FC}^{L-} = \frac{(\bar{\rho} \mathbf{U})_{f,FC}^n}{\bar{\rho}_{f,FC}^n} + \Delta t \left( -\frac{\nabla^{FC} P_{f,c}^n}{\bar{\rho}_{f,FC}^n} + \frac{\nabla^{FC} \cdot \boldsymbol{\tau}^n}{\bar{\rho}_{s,FC}} + \mathbf{b} \right) \tag{44}$$

<sup>342</sup> The equation (44) is discretized in three dimension (noted that  $\nabla^{FC} \cdot \boldsymbol{\tau} = 0$ ),  
<sup>343</sup> for example the discretized equation in the x direction is:

$$U_{fx}^{L-} = \frac{(\bar{\rho} U)_{fx,R}^n + (\bar{\rho} U)_{fx,L}^n}{\bar{\rho}_{fx,L}^n + \bar{\rho}_{fx,R}^n} + \Delta t \left( -\frac{2(v_{fx,L}^n v_{fx,R}^n)}{v_{fx,L}^n + v_{fx,R}^n} \frac{P_{f,cx,R}^n - P_{f,cx,L}^n}{\Delta x} + b_x \right) \tag{45}$$

<sup>344</sup> The cell face solid velocity can be calculated as:

$$\mathbf{U}_{s,FC}^{L-} = \frac{(\bar{\rho}\mathbf{U})_{s,FC}^n}{\bar{\rho}_{s,FC}^n} + \Delta t \left( \frac{\nabla^{FC} \cdot \boldsymbol{\sigma}_c'^n}{\bar{\rho}_{s,FC}} - \frac{\nabla^{FC} P_{f,c}^n}{\rho_s} + \mathbf{b} \right) \quad (46)$$

<sup>345</sup> The equation (46) is discretized in three dimension (noted that  $\nabla^{FC} \cdot \boldsymbol{\sigma}_{ij} = 0$   
<sup>346</sup> with  $i \neq j$ ), for example the discretized equation in the x direction is:

$$U_{sx}^{L-} = \frac{(\bar{\rho}U)_{sx,R}^n + (\bar{\rho}U)_{sx,L}^n}{\bar{\rho}_{sx,L}^n + \bar{\rho}_{sx,R}^n} + \Delta t \left( \frac{2(\sigma_{xx,R} - \sigma_{xx,L})}{(\bar{\rho}_{sx,L}^n + \bar{\rho}_{sx,R}^n)\Delta x} - \frac{P_{f,cx,R}^n - P_{f,cx,L}^n}{\rho_s \Delta x} + b_x \right) \quad (47)$$

<sup>347</sup> Then, we compute the modified cell face velocity  $\mathbf{U}_{FC}^L$  considering the mo-  
<sup>348</sup> mentum exchange (see the Appendix: Momentum exchange with an implicit  
<sup>349</sup> solve) as follows:

$$\begin{aligned} \mathbf{U}_{f,FC}^L &= \mathbf{U}_{f,FC}^{L-} + \Delta \mathbf{U}_{f,FC} \\ \mathbf{U}_{s,FC}^L &= \mathbf{U}_{s,FC}^{L-} + \Delta \mathbf{U}_{s,FC} \end{aligned} \quad (48)$$

<sup>350</sup> The linear equation below is solved to obtain the increment of velocity with  
<sup>351</sup>  $i,j = 1 : N$  as:

$$\begin{vmatrix} (1 + \beta_{ij}) & -\beta_{ij} \\ -\beta_{ji} & (1 + \beta_{ji}) \end{vmatrix} \begin{vmatrix} \Delta \mathbf{U}_{i,FC} \\ \Delta \mathbf{U}_{j,FC} \end{vmatrix} = \begin{vmatrix} \beta_{ij}(\mathbf{U}_{i,FC}^{L-} - \mathbf{U}_{j,FC}^{L-}) \\ \beta_{ji}(\mathbf{U}_{j,FC}^{L-} - \mathbf{U}_{i,FC}^{L-}) \end{vmatrix}$$

### <sup>352</sup> Compute cell face temperature

<sup>353</sup> Similar to the velocity, the faced temperature is computed, for example  
<sup>354</sup> in x direction, as:

$$\begin{aligned} T_{fx}^{L-} &= \frac{(\bar{\rho}T)_{fx,R}^n + (\bar{\rho}T)_{fx,L}^n}{\bar{\rho}_{fx,L}^n + \bar{\rho}_{fx,R}^n} \\ T_{sx}^{L-} &= \frac{(\bar{\rho}T)_{sx,R}^n + (\bar{\rho}T)_{sx,L}^n}{\bar{\rho}_{sx,L}^n + \bar{\rho}_{sx,R}^n} \end{aligned} \quad (49)$$

<sup>355</sup> Then, we compute the modified cell face temperature  $T_{FC}^L$  considering the  
<sup>356</sup> energy exchange (see the Appendix: Momentum and energy exchange with  
<sup>357</sup> an implicit solver) as follows:

$$\begin{aligned} T_{f,FC}^L &= T_{f,FC}^{L-} + \Delta T_{f,FC} \\ T_{s,FC}^L &= T_{s,FC}^{L-} + \Delta T_{s,FC} \end{aligned} \quad (50)$$

<sup>358</sup> The linear equation below is solved to determine the increment of velocity  
<sup>359</sup> with  $i,j = 1 : N$  as:

$$\begin{vmatrix} (1 + \eta_{ij}) & -\eta_{ij} \\ -\eta_{ji} & (1 + \eta_{ji}) \end{vmatrix} \begin{vmatrix} \Delta T_{i,FC} \\ \Delta T_{j,FC} \end{vmatrix} = \begin{vmatrix} \eta_{ij}(T_{i,FC}^{L-} - T_{j,FC}^{L-}) \\ \eta_{ji}(T_{j,FC}^{L-} - T_{i,FC}^{L-}) \end{vmatrix}$$

360    ***Compute fluid pressure (implicit scheme)***

361    For single phase flow, the increment of the fluid pressure can be computed  
362    as:

$$\kappa_f \frac{\Delta P}{dt} = \nabla^c \cdot \mathbf{U}_{f,FC}^{n+1} \quad (51)$$

363    For multi-phase flows, the increment of the fluid pressure of the mixture can  
364    be computed as:

$$\kappa \frac{\Delta P}{dt} = \sum_{f=1}^{N_f} \nabla^c \cdot (\phi_{f,FC} \mathbf{U}_{f,FC})^{n+1} \quad (52)$$

365    where  $\kappa = \sum_{f=1}^{N_f} (\phi_{f,FC} \kappa_f) / \sum_{f=1}^{N_f} (\phi_{f,FC})$ . Then, the fluid pressure at cell  
366    center is:

$$P_c^{n+1} = P_c^n + \Delta P_c^n \quad (53)$$

367    Finally, the cell face advanced fluid pressure is:

$$P_{FC}^{n+1} = \left( \frac{P_{c,L}^{n+1}}{\bar{\rho}_{f,L}^n} + \frac{P_{c,R}^{n+1}}{\bar{\rho}_{f,R}^n} \right) / \left( \frac{1}{\bar{\rho}_{f,L}^n} + \frac{1}{\bar{\rho}_{f,R}^n} \right) = \left( \frac{P_{c,L}^{n+1} \bar{\rho}_{f,R}^n + P_{c,R}^{n+1} \bar{\rho}_{f,L}^n}{\bar{\rho}_{f,L}^n \bar{\rho}_{f,R}^n} \right) \quad (54)$$

368    ***Compute viscous shear stress term of the fluid phase***

369    This part compute the viscous shear stress  $\Delta(m\mathbf{U})_{f,c,\tau}$  for a single vis-  
370    cous compressible Newtonian fluid and optionally shear stress induced by the  
371    turbulent model.

372    ***Compute nodal internal temperature of the solid phase***

373    The nodal internal temperature rate is computed based on the heat con-  
374    duction model as below:

$$dT_{si}^{L-} = \frac{(\Delta W_{si}^n + \Delta W_{fric,i}^n + \nabla^i \cdot \mathbf{q}_{si}^n)}{m_{si}^n c_v} \quad (55)$$

375    where  $\Delta W_{si}^n = \boldsymbol{\sigma}' : \frac{D_s(\boldsymbol{\epsilon}_s^p)}{Dt}$  is the mechanical work rate computed from the  
376    constitutive model with  $\boldsymbol{\epsilon}_s^p$  is the plastic strain,  $\Delta W_{fric,i}^n$  is the work rate  
377    computed from the contact law due to the frictional sliding between solid  
378    materials. The heat flux is  $\mathbf{q}_s = \bar{\rho}_s \beta_s \nabla T_s$  with  $\beta_s$  being the thermal conduc-  
379    tivity of the solid materials.

$$T_{si}^{L-} = T_{si}^n + dT_{si}^{L-} \quad (56)$$

### 380 *Compute and integrate acceleration of the solid phase*

After interpolating from material points to the nodes, the nodal acceleration and velocity are calculated by:

$$\mathbf{a}_{si}^{L-} = \frac{\mathbf{f}_{si}^{int,n} + \mathbf{f}_{si}^{ext,n}}{m_{si}^n} + \mathbf{g} \quad (57)$$

$$U_{si}^{L-} = U_{si}^n + a_{si}^{L-} \Delta t \quad (58)$$

384 Compute Lagrangian value (mass, momentum and energy)

For the fluid phase, the linear momentum rate, the energy rate are:

$$\Delta(m\mathbf{U})_{f,c} = Vn_c^n \nabla^c P_c^{n+1} + \Delta(m\mathbf{U})_{f.c,\tau} + V\bar{\rho}_{f,c}^n g \quad (59)$$

$$\Delta(me)_{f,c} = V n_c^n P_c^{n+1} \nabla^c \cdot \mathbf{U}_{f,FC}^* + \nabla^c \cdot \mathbf{q}_{f,c}^n \quad (60)$$

387 The Lagrangian value of the mass, linear momentum and energy of fluid  
388 phases without momentum exchange are:

$$m_{f,c}^L = V \bar{\rho}_{f,c}^n \quad (61)$$

$$(m\mathbf{U})_{f,c}^{L-} = V \bar{\rho}_{f,c}^n \mathbf{U}_{f,c}^n + \Delta(m\mathbf{U})_{f,c} \quad (62)$$

$$(me)_{fc}^{L-} = V \bar{\rho}_{fc}^n T_{fc}^n c_v + \Delta(me)_{fc} \quad (63)$$

391 For the solid phase, the Lagrangian value of the linear momentum and energy  
392 of solid phase are:

$$m_{sc}^L = m_{sc}^n \quad (64)$$

$$(m\mathbf{U})_{sc}^{L-} = \sum S_{ci} m_{si}^n \mathbf{U}_{si}^{L-} + V(1 - n_c^n) \nabla^c P_f^{n+1} \quad (65)$$

$$(me)_{ci}^{L-} \equiv \sum S_{ci} m_{ci}^n T_{ci}^L c_v \quad (66)$$

<sup>395</sup> To consider the momentum exchange, the Lagrangian velocity is modified as:

$$\begin{aligned} \mathbf{U}_{f,c}^L &= \mathbf{U}_{f,c}^{L-} + \Delta \mathbf{U}_{f,c} \\ \mathbf{U}_{s,c}^L &= \mathbf{U}_{s,c}^{L-} + \Delta \mathbf{U}_{s,c} \end{aligned} \quad (67)$$

where the cell-centered intermediate velocity can be calculated by:

$$\begin{aligned} \mathbf{U}_{f,c}^{L-} &= \frac{(m\mathbf{U})_{f,c}^{L-}}{m_{f,c}^L} \\ \mathbf{U}_{sc}^{L-} &= \frac{(m\mathbf{U})_{sc}^{L-}}{m_{sc}^L} \end{aligned} \quad (68)$$

<sup>397</sup> And the increment of the velocity  $\mathbf{U}_{f,c}$ ,  $\Delta\mathbf{U}_{sc}$  can be computed by solving  
<sup>398</sup> the linear equation with  $i,j = 1 : N$  as:

$$\begin{vmatrix} (1 + \beta_{ij}) & -\beta_{ij} \\ -\beta_{ji} & (1 + \beta_{ji}) \end{vmatrix} \begin{vmatrix} \Delta\mathbf{U}_{i,c} \\ \Delta\mathbf{U}_{j,c} \end{vmatrix} = \begin{vmatrix} \beta_{ij}(\mathbf{U}_{i,c}^{L-} - \mathbf{U}_{j,c}^{L-}) \\ \beta_{ji}(\mathbf{U}_{j,c}^{L-} - \mathbf{U}_{i,c}^{L-}) \end{vmatrix}$$

<sup>399</sup> To consider the energy exchange, the Lagrangian temperature is modified as:

$$\begin{aligned} T_{f,c}^L &= T_{f,c}^{L-} + \Delta T_{f,c} \\ T_{sc}^L &= T_{sc}^{L-} + \Delta T_{sc} \end{aligned} \quad (69)$$

<sup>400</sup> where the cell-centered intermediate temperature can be calculated by:

$$\begin{aligned} T_{f,c}^{L-} &= \frac{(mT)_{f,c}^{L-}}{m_{f,c}^L c_v} \\ T_{sc}^{L-} &= \frac{(mT)_{sc}^{L-}}{m_{sc}^L c_v} \end{aligned} \quad (70)$$

<sup>401</sup> And the increment of the velocity can be computed by solving the linear  
<sup>402</sup> equation with  $i,j = 1 : N$  as:

$$\begin{vmatrix} (1 + \eta_{ij}) & -\eta_{ij} \\ -\eta_{ji} & (1 + \eta_{ji}) \end{vmatrix} \begin{vmatrix} \Delta T_{i,c} \\ \Delta T_{j,c} \end{vmatrix} = \begin{vmatrix} \eta_{ij}(T_{i,c}^{L-} - T_{j,c}^{L-}) \\ \eta_{ji}(T_{j,c}^{L-} - T_{i,c}^{L-}) \end{vmatrix}$$

<sup>403</sup> Finally, we obtain the cell-centered solid acceleration and temperature rate  
<sup>404</sup> as:

$$d\mathbf{U}_{sc}^L = \frac{(m\mathbf{U})_{sc}^L - (m\mathbf{U})_{sc}^n}{m_{sc}^L \Delta t} \quad (71)$$

$$dT_{sc}^L = \frac{(me)_{sc}^L - (me)_{sc}^n}{m_{sc}^L c_v \Delta t} \quad (72)$$

#### <sup>406</sup> Compute Lagrangian specific volume of the fluid phase

<sup>407</sup> To compute the Lagrangian value of the specific volume of the fluid phase,  
<sup>408</sup> we need to compute the Lagrangian temperature rate as below:

$$T_{f,c}^{n+1} = \frac{(me)_{f,c}^L}{m_{f,c}^L c_v} \quad (73)$$

$$\frac{D_f T_{f,c}}{Dt} = \frac{T_{f,c}^{n+1} - T_{f,c}^n}{\Delta t} \quad (74)$$

<sup>410</sup> As such, the Lagrangian specific volume rate is:

$$\Delta(mv)_{f,c} = V f_{f,c}^\phi \nabla \cdot \mathbf{U} + (\phi_{f,c} \alpha_{f,c} \frac{D_f T_{f,c}}{Dt} - f_{f,c}^\phi \sum_{n=1}^N \phi_{nc} \alpha_{nc} \frac{D_n T_{n,c}}{Dt}) \quad (75)$$

<sup>411</sup> where  $f_f^\phi = (\phi_f \kappa_f) / (\sum_{n=1}^N \phi_n \kappa_n)$  and  $\mathbf{U} = \nabla \cdot (\sum_{s=1}^{N_s} \phi_{sc} \mathbf{U}_{sc} + \sum_{f=1}^{N_f} \phi_{fc} \mathbf{U}_{f,c})$ .

<sup>412</sup> Finally, the Lagrangian specific volume is:

$$(mv)_{f,c}^L = V \bar{\rho}_{f,c}^n v_{f,c}^n + \Delta(mv)_{f,c} \quad (76)$$

<sup>413</sup> *Compute advection term and advance in time*

<sup>414</sup> The time advanced mass, linear momentum, energy and specific volume  
<sup>415</sup> are:

$$m_{f,c}^{n+1} = m_{f,c}^L - \Delta t \nabla \cdot (\bar{\rho}_{f,c}^L, \mathbf{U}_{f,FC}^L) \quad (77)$$

$$(m\mathbf{U})_{f,c}^{n+1} = (m\mathbf{U})_{f,c}^L - \Delta t \nabla \cdot ((\bar{\rho}\mathbf{U})_{f,c}^L, \mathbf{U}_{f,FC}^L) \quad (78)$$

$$(me)_{f,c}^{n+1} = (me)_{f,c}^L - \Delta t \nabla \cdot ((\bar{\rho}c_v T)_{f,c}^L, \mathbf{U}_{f,FC}^L) \quad (79)$$

$$(mv)_{f,c}^{n+1} = (mv)_{f,c}^L - \Delta t \nabla \cdot ((\bar{\rho}v)_{f,c}^L, \mathbf{U}_{f,FC}^L) \quad (80)$$

<sup>419</sup> Finally, the state variables of the fluid phases of the next time step are:

$$\bar{\rho}_{f,c}^{n+1} = \frac{m_{f,c}^{n+1}}{V} \quad (81)$$

$$\mathbf{U}_{f,c}^{n+1} = \frac{(m\mathbf{U})_{f,c}^{n+1}}{m_{f,c}^{n+1}} \quad (82)$$

$$T_{f,c}^{n+1} = \frac{(me)_{f,c}^{n+1}}{m_{f,c}^{n+1}} \quad (83)$$

$$v_{f,c}^{n+1} = \frac{(mv)_{f,c}^{n+1}}{m_{f,c}^{n+1}} \quad (84)$$

423    *Interpolate from cell to node of the solid phase*

424    First we interpolate the acceleration, velocity and temperature rate to  
425    the node as below:

$$426 \quad \mathbf{a}_{si}^n = \sum S_{ci} d\mathbf{U}_{sc}^L \quad (85)$$

$$426 \quad \mathbf{U}_{si}^{n+1} = \sum S_{ci} d\mathbf{U}_{sc}^L \Delta t \quad (86)$$

$$427 \quad dT_{si}^n = \sum S_{ci} dT_{sc}^L \quad (87)$$

428    Then the boundary condition and contact forces  $f_{si}^{fric}$  are applied to the nodal  
429    velocity and the acceleration is modified by:

$$429 \quad \mathbf{a}_{si}^n = \frac{\mathbf{v}_{si}^{n+1} - \mathbf{v}_{si}^n}{\Delta t} \quad (88)$$

430    *Update the particle variables*

431    The state variables of the solid phase  $[\mathbf{U}_{sp}^{n+1}, \mathbf{x}_{sp}^{n+1}, \nabla \mathbf{U}_{sp}^{n+1}, T_{sp}^{n+1}, \nabla T_{sp}^{n+1}, \mathbf{F}_{sp}^{n+1}, V_{sp}^{n+1}]$   
432    (velocity, position, velocity gradient, temperature, temperature gradient, de-  
433    formation gradient, volume) are updated as:

$$434 \quad \mathbf{U}_{sp}^{n+1} = \mathbf{U}_{sp}^n + \sum S_{sp} \mathbf{a}_{si}^n \Delta t \quad (89)$$

$$435 \quad \mathbf{x}_{sp}^{n+1} = \mathbf{x}_{sp}^n + \sum S_{sp} \mathbf{U}_{si}^{n+1} \Delta t \quad (90)$$

$$436 \quad \nabla \mathbf{U}_{sp}^{n+1} = \sum \nabla S_{sp} \mathbf{U}_{si}^{n+1} \quad (91)$$

$$437 \quad T_{sp}^{n+1} = T_{sp}^n + \sum S_{sp} dT_{si}^n \Delta t \quad (92)$$

$$438 \quad \nabla T_{sp}^{n+1} = \sum \nabla S_{sp} T_{sp}^n \Delta t \quad (93)$$

$$439 \quad \mathbf{F}_{sp}^{n+1} = (\mathbf{I} + \nabla \mathbf{U}_{sp}^{n+1} \Delta t) \mathbf{F}_{sp}^n \quad (94)$$

$$439 \quad V_{sp}^{n+1} = \det(\mathbf{F}_{sp}^{n+1}) V_{sp}^o \quad (95)$$

440    Finally, the effective stress  $(\boldsymbol{\sigma}')^{n+1}$  is updated from the constitutive model  
441    and the pore water pressure is interpolated from the cell as:

$$442 \quad p_f^{n+1} = \sum S_{si} P_c^{n+1} \quad (96)$$

442 **Numerical examples**

443 All input files and the analytical calculations in this section are provided  
 444 in the Github repository ([https://github.com/QuocAnh90/Uintah\\_NTNU](https://github.com/QuocAnh90/Uintah_NTNU))  
 445 for the reproduction of the numerical results.

446 To prevent repetition, we present the parameters of water and air, which  
 447 remain consistent across all simulations. The water has a bulk modulus of 2  
 448 GPa, a density of 998 kg/m<sup>3</sup> at a reference temperature of 5 degrees Celsius  
 449 and a reference pressure of 10325 Pa (1atm), a dynamic viscosity  $\mu_f$  of 1  
 450 mPa s). The air has a ideal gas with a density of 1.17 kg/m<sup>3</sup> at a reference  
 451 temperature of 5 degrees Celsius and a reference pressure of 10325 Pa (1atm),  
 452 a dynamic viscosity  $\mu_f$  of  $18.45E^{-3}$  mPa s).

453 *Fluid Flow through isothermal porous media*

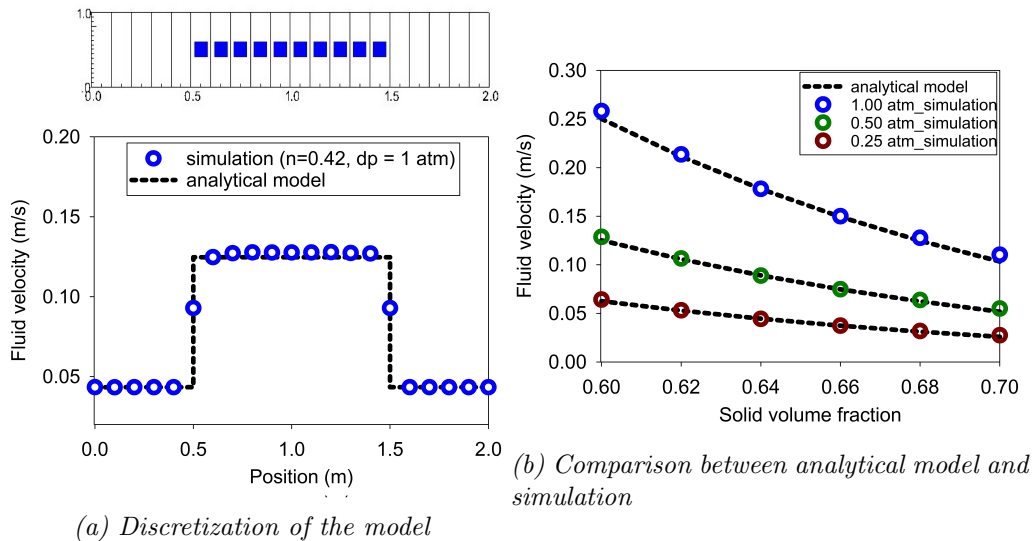


Figure 7: Numerical results of the fluid flow through isothermal porous media

454 Fluid flow through porous media is important in many engineering disci-  
 455 plines, like predicting water flow in soil. Fluid flow velocity in one dimension  
 456 can be calculated from the porous media's hydraulic conductivity  $K$  as:

457

$$U_f = K \frac{\Delta p_f}{L} \quad (97)$$

458 If the Carman-Kozeny formula is adopted  $F = 10\phi_s/(1 - \phi_s)^2$ , the hydraulic  
 459 conductivity will be expressed as  $K = D_p^2(1 - \phi_s)^3\rho_f g/180\phi_s^2\mu_f$ . Then, the  
 460 analytical formula of average velocity in one dimension through the porous  
 461 media is:

462

$$U_f = \frac{1}{n} \frac{D_p^2(1 - \phi_s)^3}{180\phi_s^2\mu_f} \frac{\Delta p_f}{L} \quad (98)$$

463 Our numerical model is validated by modeling fluid flow through a 1m  
 464 long porous media. The porous media is modeled by elastic material with  
 465 Young's modulus is 10 MPa, Poisson's ratio is 0.3, and density is 2650 kg/m<sup>3</sup>.  
 466 The volume fraction of porous media  $\phi_s$  is [0.6, 0.62, 0.66, 0.68, 0.7] and the  
 467 average grain diameter  $d$  is 1mm. The model is discretized in 20 finite element  
 468 and the porous media in 10 finite element with 1 material point per element.  
 469 The pressure gradient is applied with three different value [0.25, 0.5, 1] atm.  
 470 Figure 7 shows a good agreement of fluid flow prediction between the theory  
 471 and the model.

472 *Isothermal consolidation*

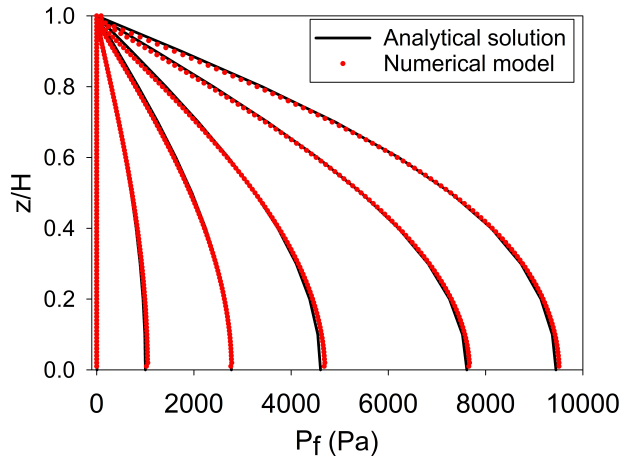


Figure 8: Comparison between analytical solution and numerical solution

473 A common benchmark for a fully saturated porous media is the simulation  
 474 of one-dimensional consolidation. Using the Carman-Kozeny formula, the

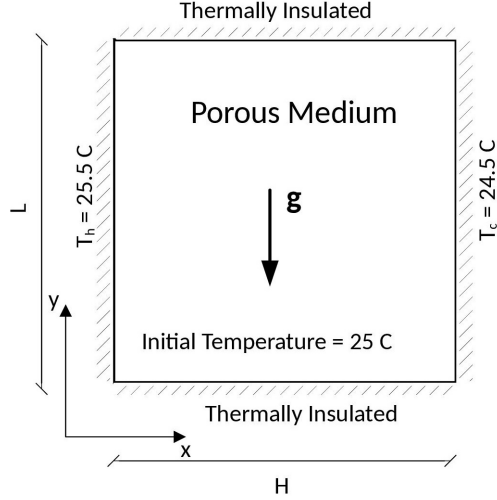


Figure 9: Model schematic [23]

475 time-dependent pressure can be calculated as:

$$p_f = \sum_{m=1}^{\infty} \frac{2F_{ext}}{M} \sin\left(\frac{Mz}{H}\right) e^{-M^2 T_v} \text{ with } M = \frac{\pi}{2}(2m+1) \quad (99)$$

476 where the consolidation rate  $T_v = C_v t / H^2$ , the consolidation coefficient  $C_v =$   
 477  $E_v n^3 d^2 / (180(1-n)^2 \mu)$  and the Oedometer modulus  $E_v = E(1-v)/(1+v)/(1-2v)$ . Our numerical model is validated by modeling the consolidation  
 478 of a 1m column. The porous media is modeled by elastic material with  
 480 Young's modulus is 10 MPa, Poisson's ratio is 0.3, and density is 2650 kg/m<sup>3</sup>.  
 481 The volume fraction of porous media  $\phi_s$  is 0.7 which is equivalent to the  
 482 porosity of 0.3 and the average grain diameter  $d$  is 1mm. The model is  
 483 discretized in 100 finite element with 1 material point per element. The  
 484 external pressure applies to the top of the column is 10 kPa. Figure 8 shows  
 485 a good agreement of fluid flow prediction between the theory and the model.

486 *Thermal induced cavity flow*

487 Another benchmark is the thermal induced cavity flow in porous me-  
 488 dia. Temperature and velocity distributions are calculated for a square non-  
 489 deformable saturated porous media. The top and bottom walls are insulated,  
 490 and the left and right walls are at fixed temperature gradient of 1 degree. The  
 491 fluid motion at steady state are cavity flow due to the temperature induced

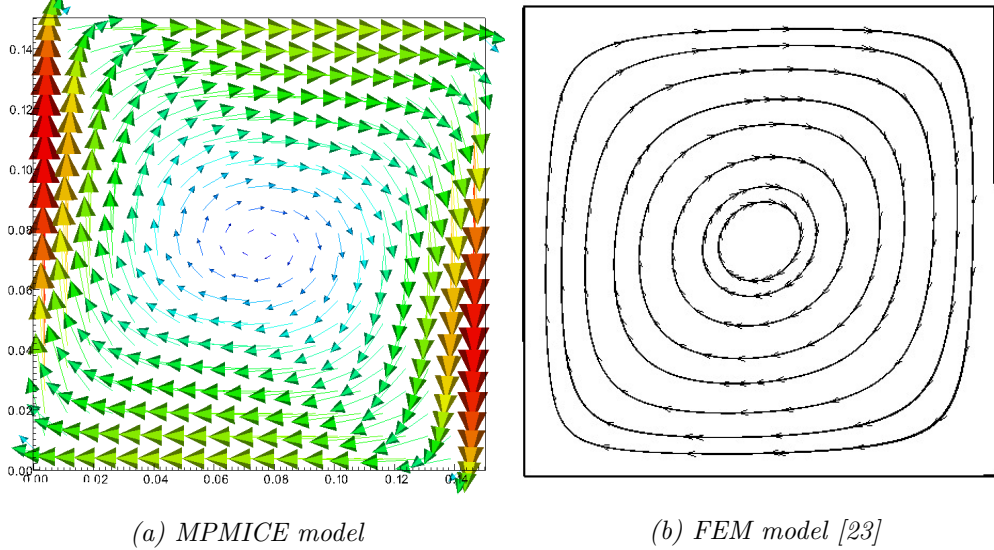
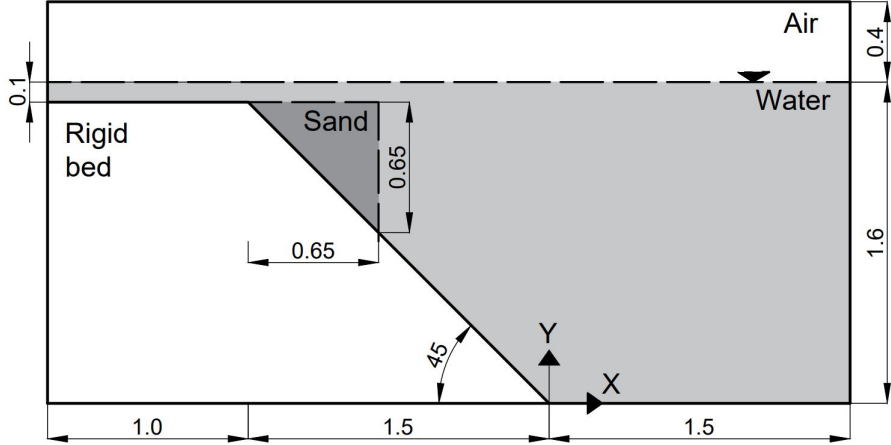


Figure 10: Comparison between MPMICE model and FEM model

density variation. The numerical is validated by comparing with the numerical solution of the finite element method. The porous media is modeled by non deformable material, and density is 2500 kg/m<sup>3</sup>. The specific heat capacity of the water and porous skeleton are 4181 J/kg.K and 835 J/kg.K respectively. The thermal conductivity of the water and porous skeleton are 0.598 W/m.K and 0.4 W/m.K. The volume fraction of porous media  $\phi_s$  is 0.6 which is equivalent to the porosity of 0.4 and the average grain diameter  $d$  is 1mm. The model is discretized in 20 x 20 finite element with 4 material point per element. Figure 10 shows a good agreement of numerical results of the model compared with the numerical solution of the finite element method.

#### Underwater debris flow

The numerical example is validated using the experimental work of Rzadkiewicz et al. on submarine debris flow [24]. In their experiment, sand within a triangular box is released and slides along a rigid bed inclined at 45 degrees under water (see Figure 11). The material properties in the numerical model are selected based on the experiment by Rzadkiewicz et al. [24]. The sand is characterized by a saturated density of 1985 kg/m<sup>3</sup> and a friction angle of 10 degrees. The effect of Young's modulus on debris flow run-out is negligible due to the extreme deformation of the debris, so a Young's modulus



*Figure 11: Model schematic*

of 50 MPa with a Poisson's ratio of 0.25 is chosen. The rigid bed, being much stiffer, has bulk modulus and shear modulus values of  $117E^7$  Pa and  $43.8E^7$  Pa, respectively. The numerical parameters used in this example are presented in Table 1.

The boundary conditions imposed in the numerical model are as follows: on all boundary faces, the velocity is set to zero ( $U = 0$  m/s) and the temperature is set to 5 degrees Celsius ( $T = 5^\circ\text{C}$ ). At the top boundary, the pressure has a Neumann boundary condition of  $dP/dx = 0$  kPa, and the density has a Neumann boundary condition of  $d\rho/dx = 0 \text{ kg/m}^3$ . The background mesh consists of  $700 \times 400$  cells, resulting in a total of 280,000 cells. Each cell in the debris flow and rigid bed contains  $2 \times 2$  material points.

Figure 13b illustrates snapshots of the underwater debris flow sliding, demonstrating that the model captures the typical hydroplaning mechanism of the debris flow. Hydroplaning refers to the lifting of the debris flow, causing it to lose contact with the bottom layer. The elevation of the free surface at 0.4s and 0.8s is compared between our proposed method and other methods in Figure 12. Our computed results align well with the experimental results [7].

Unlike other computational models that rely on total stress analysis [5, 6, 7, 8], our proposed model utilizes effective stress analysis, enabling the analysis of water pressure and temperature within the debris flow. Additionally, we investigate the differences between underwater debris flow and saturated debris flow in terms of their interaction with obstacles. Figure 13 presents

534 snapshots of simulations of both underwater and saturated debris flow. The  
 535 saturated debris flow (Figure 13a) exhibits behavior similar to frictional flow,  
 536 where grains have contact forces with each other. Conversely, the underwa-  
 537 ter debris flow (Figure 13b) behaves like turbulent flow, with grains being  
 538 separated from each other and exhibiting no contact forces (as reflected by  
 the near-zero effective stress in the turbulence domain).

Materials	Bulk modul (Pa)	Shear modul (Pa)	Density (kg/m <sup>3</sup> )	Temp (C)	Dynamic viscosity (Pa s)	Friction angle (degrees)
Water (at surface)	2.15e9	-	999.8	5	855e-6	-
Air (at top boundary)	-	-	1.177	5	18.45e-6	-
Sand (porous media)	8.33e6	20e6	1985	5	-	10
Rigid bed (solid)	117e7	43.8e7	8900	5	-	-

Table 1: Numerical parameters for the underwater submarine debris

539

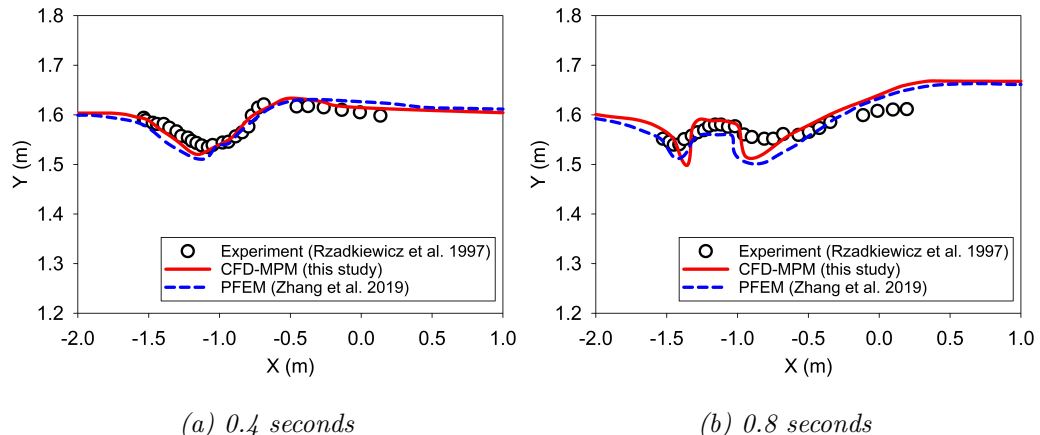


Figure 12: Evolution of water level in the simulation of underwater debris flow

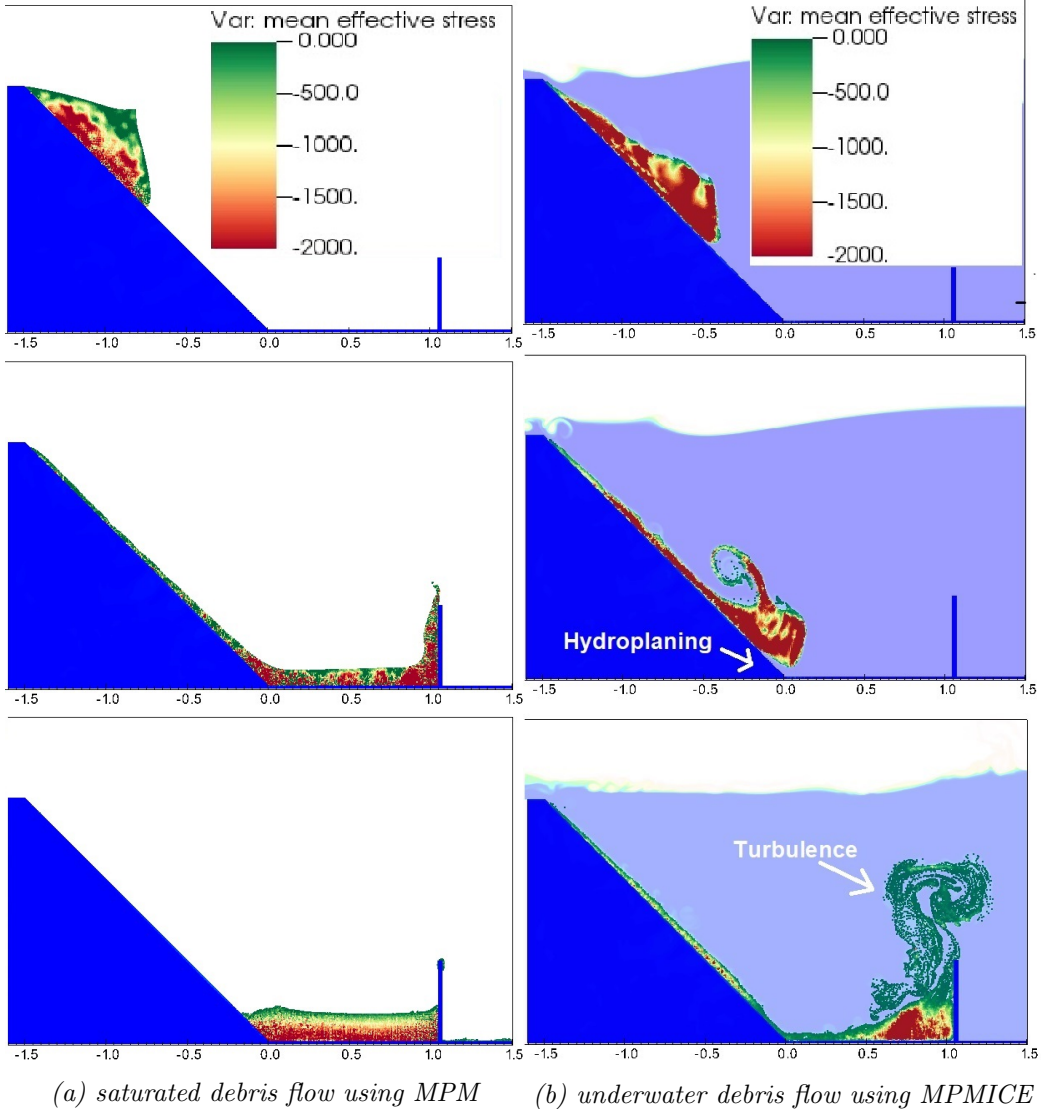
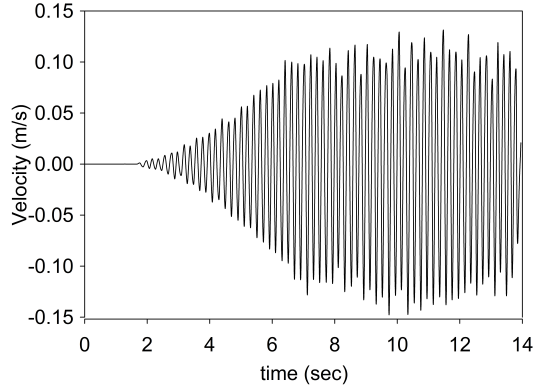
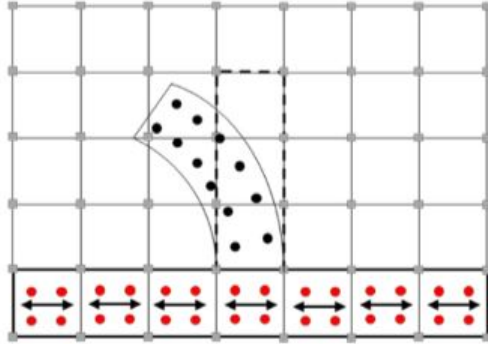


Figure 13: Simulation of Debris Flow: Mean Effective Stress Distribution (Green Color Indicates Near-Zero Effective Stress)

540    *Validation of soil response to the seismic loading*



*Figure 14: Seismic loading*



*Figure 15: Material points prescribed velocity as kinematic boundary condition [25]*

541    An experimental study conducted by Hiraoka et al. [26] aimed to inves-  
 542    tigate the influence of seismic shaking on the deformation of a 0.5 m-high  
 543    sand slope. The sand used in the experiment was partially saturated, with a  
 544    moisture content of 10 percent. The provided soil parameters for the Mohr  
 545    Coulomb model include the effective friction angle of 23 degrees, apparent  
 546    cohesion of 0.78 kPa, Young's modulus of 2.57 MPa, and Poisson's ratio of  
 547    0.33, and moist unit weight of 16.5 kN/m<sup>3</sup>. The soil's dilatancy angle was  
 548    assumed to be 0 [26]. The experimental setup consisted of a shaking table  
 549    box with a steel horizontal base and smooth glass vertical sidewalls. Laser

550 sensors were used to monitor the displacement of the slope's toe and crest.  
551 Figure 14 displays the velocity-time history employed in the experiment.

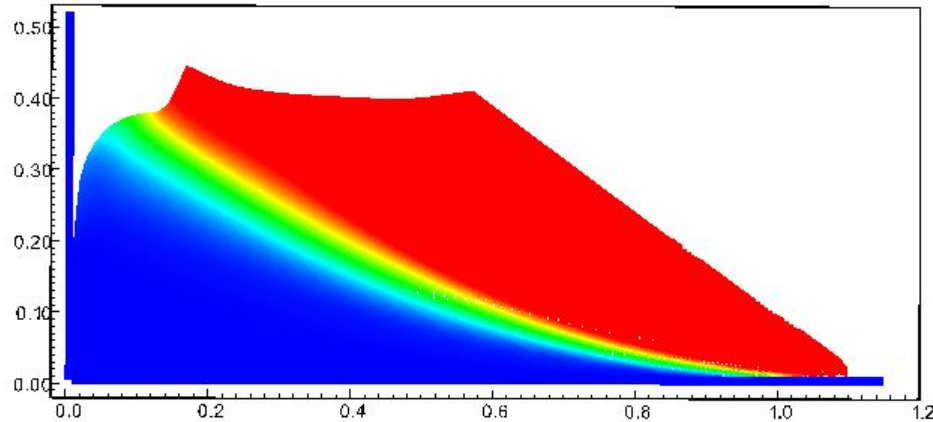


Figure 16: Numerical model of the seismic-induced slope failure with displacement color

552 To simulate the seismic loading in our numerical model, we adopted a  
553 method presented by Alsardi et al. [25], which involves specifying the velocity  
554 at the corresponding material points representing either the shaking table or  
555 the bedrock at the site (see Figure 15). In our simulation, we considered the  
556 horizontal base to be fully rough and the vertical contact to be fully smooth.  
557 The initial stress condition was initiated using gravity and seismic loading  
558 induced the slope failure (see Figure 16).  
559 Previous studies by Bhandari et al. [27], Alsardi et al. [25], and Hiraoka et  
560 al. [26] attempted to model this experiment using MPM and SPH models. In  
561 this study, we compared our results with those obtained from other particle-  
562 based methods (Figure 17). The main difference is that we did not apply  
563 5 percent numerical damping in our model, unlike the other methods. We  
564 found that the final displacement of the slope toe in our MPM model was  
565 higher than that observed in the experiment. Nevertheless, the validation of  
566 the Mohr-Coulomb model under seismic response demonstrated a reasonable  
567 soil behavior in terms of displacement.

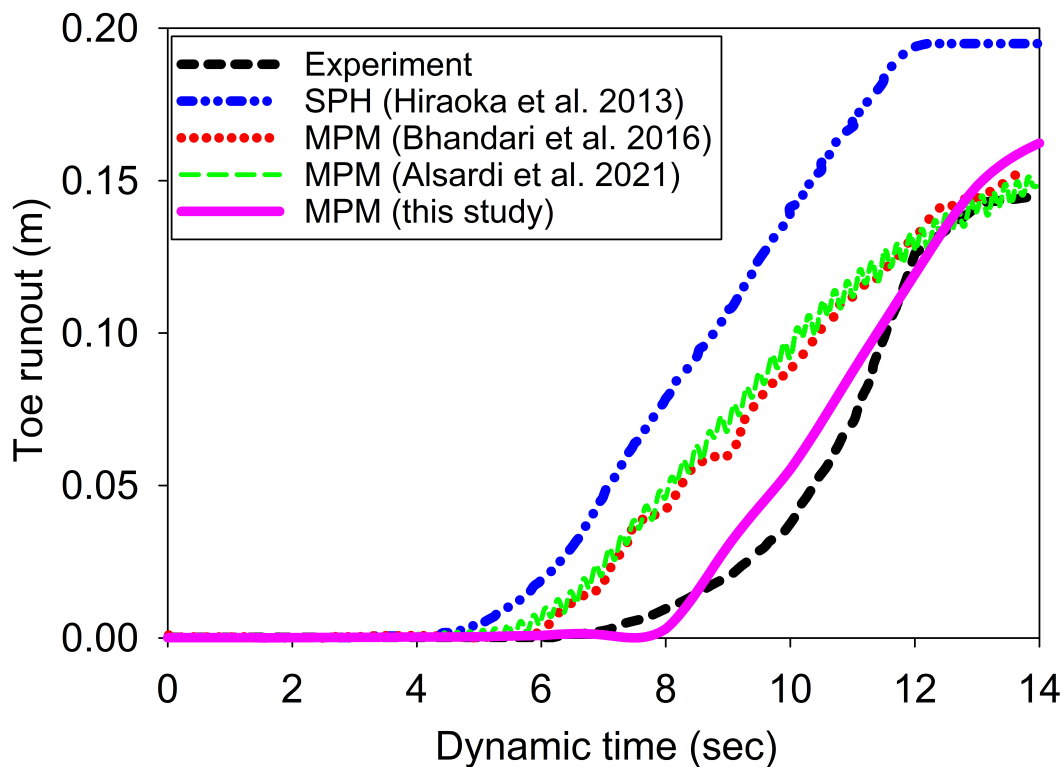


Figure 17: Displacement of the toe of the slope

568 *Earthquake-induced submarine landslides*

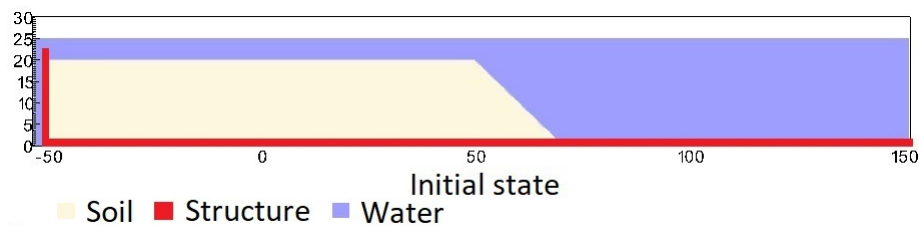
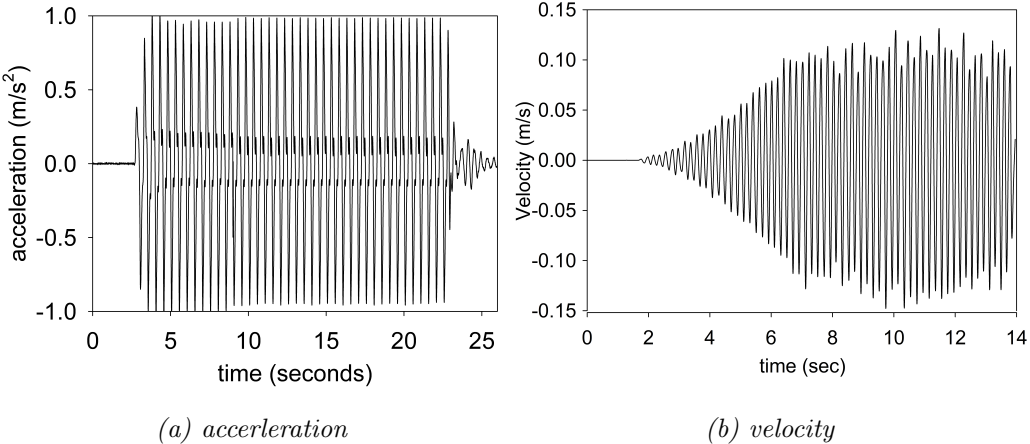


Figure 18: Numerical simulation of the earthquake-induced submarine landslide



*Figure 19: Ground acceleration profile, frequency of 2Hz and magnitude of 1g*

569 In the final example, we perform numerical analysis of the earthquake  
 570 induced submarine landslides. A plane strain model with the slope under  
 571 water is shown in Figure 18. A 20m high slope with slope gradient of 45  
 572 degrees is placed in a horizontal and vertical structure which was used to  
 573 be a scaling table to apply earthquake loading. We simplify the earthquake  
 574 loading by simulating the ground shaking for 20 seconds with the constant  
 575 ground acceleration of 1g and a constant frequency of 2Hz (Figure 19a). The  
 576 ground motion is applied in terms of velocity (Figure 19b). An earthquake  
 577 of this magnitude is possible. For instance, in the case of the 2023 Turkey-  
 578 Syria Earthquake, significant ground shaking with peak ground acceleration  
 579 exceeding 1g was observed at numerous locations. This serves as an example  
 580 of the practical occurrence of such high levels of ground acceleration during  
 581 seismic events. To generate the seismic loading, the same method was used  
 582 as presented in the previous numerical example.

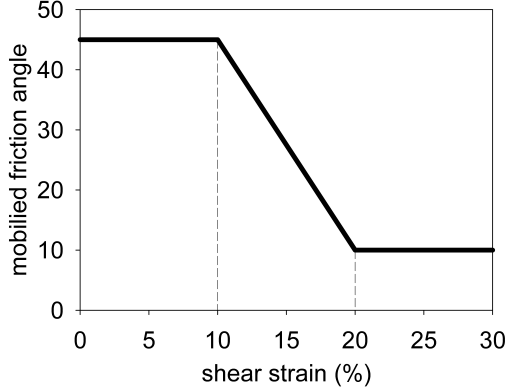
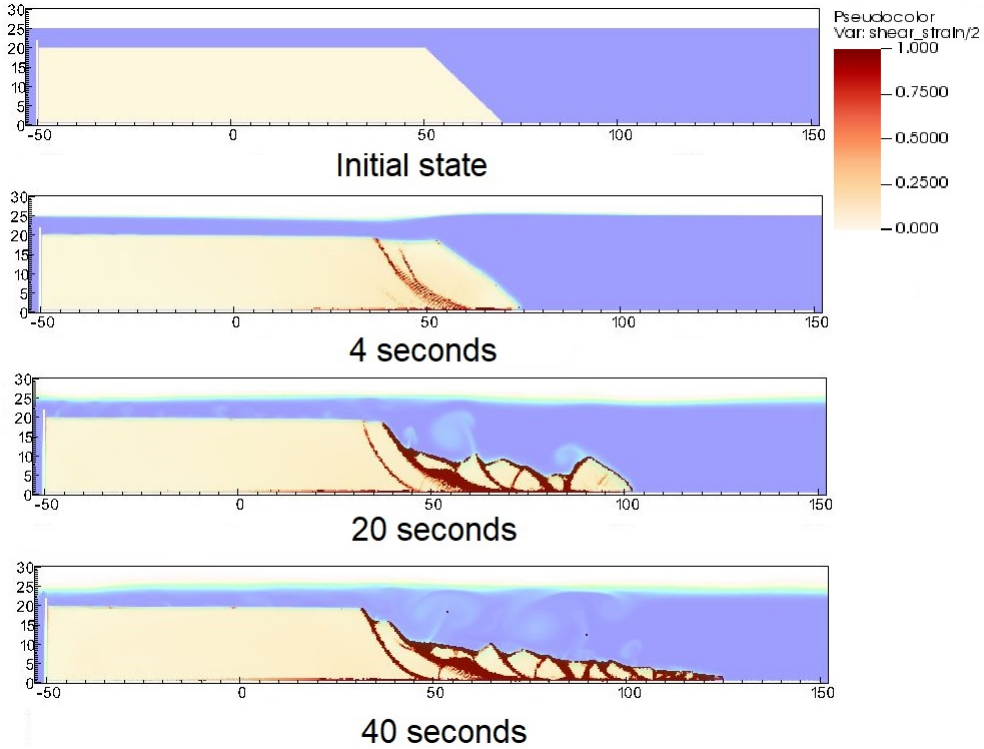


Figure 20: Mobilized friction angle in Mohr Coulomb model

583 A non-associated Mohr-Coulomb model is used for the soil. The soil grain  
 584 has the density of  $2650 \text{ kg/m}^3$ , Young's modulus of 10 kPa and Poisson's  
 585 ratio of 0.3 and zero cohesion. The mobilized friction angle  $\phi'_m$  is governed  
 586 following the softening curve (see Figure 20) with the peak friction angle  $\phi'_p$   
 587 of 45 degrees and the residual friction angle  $\phi'_r$  of 10 degrees. The porosity  
 588 is 0.3 and the average grain size of the soil is around  $0.1 \mu\text{m}$  to mimic the  
 589 undrained behavior. The mobilized dilatancy angle is calculated from the  
 590 Rowe's stress dilatancy theory [28] as follow:

$$\sin \psi'_m = \frac{\sin \phi'_m - \sin \phi'_r}{1 - (\sin \phi'_r \sin \phi'_m)} \quad (100)$$

591 The solid plane is modeled as a rigid body acted as a shaking table. The  
 592 contact between horizontal plane and the sand is the frictional contact with  
 593 the friction coefficient of 0.1. No artificial damping is applied in the simu-  
 594 lation. The contact between vertical plane and the sand is considered to be  
 595 smooth with zero friction coefficient. On all boundary faces, the symmet-  
 596 ric boundary condition is imposed, while the Neumann boundary condition  
 597 is imposed at the top boundary for pressure ( $d\rho/dx = 0 \text{ kPa}$ ) and density  
 598 ( $d\rho/dx = 0 \text{ kg/m}^3$ ). Symmetric boundary condition refers to a condition  
 599 where the normal component of the velocity at the boundary face is set to  
 600 zero, and the tangential component is equal to the tangential component of  
 601 the neighboring cells. The mesh size is  $0.25 \times 0.25 \text{ m}$  with 300852 element  
 602 cells and 142316 material points. The simulation takes a couple of hours to  
 603 perform 60 seconds of the simulation using 4096 CPUs.



*Figure 21: Shear strain during the earthquake-induced submarine landslides*

We demonstrate the entire process and the mechanism of the earthquake-induced submarine landslides by showing the shear strain (Figure 21), the pore water pressure in atm (Figure 22) and the velocity (Figure 23). The failure mechanism can be characterized as the progressive failure mechanism. Here are some numerical observation:

- At the initial of the seismic event, the seismic loading triggers the first slide at 3 seconds. At 4 seconds, the debris start to move with the maximum speed of around 2-3 m/s with multiple shear band developed in the slope. The wave generated from the submarine slide is around 2-3m towards the slide direction.

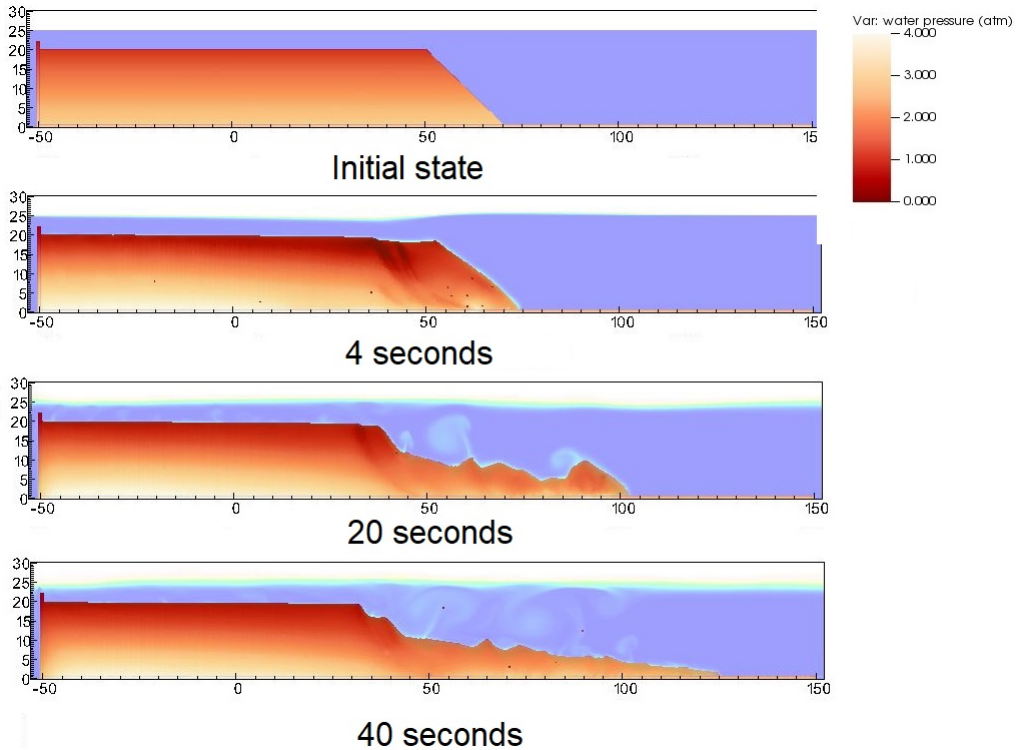


*Figure 22: pore water pressure during the earthquake-induced submarine landslides*

- 614     2. When the onset of the shear band occurs in the slope (for example  
615       at 4 seconds and 20 seconds), the negative excess pore water pressure  
616       is developed along this shear band with pore water pressure is under  
617       1atm. This is a typical dilatancy behavior when the soil is sheared  
618       rapidly in the undrained behavior.
- 619     3. When the seismic loading ends at 23 seconds, the last shear band is  
620       mobilized and the slope soon reaches to the final deposition. No more  
621       progressive failure developed in the slope. The turbulent flow developed  
622       as the interaction between debris flow and seawater.
- 623     Overall, we show the completed process of the earthquake-induced submarine  
624       landslides involving (1) earthquake triggering mechanism, (2) the onset of the  
625       shear band with the development of negative excess pore water pressure, (3)  
626       progressive failure mechanism, (4) submarine landslide induced wave to final  
627       deposition.

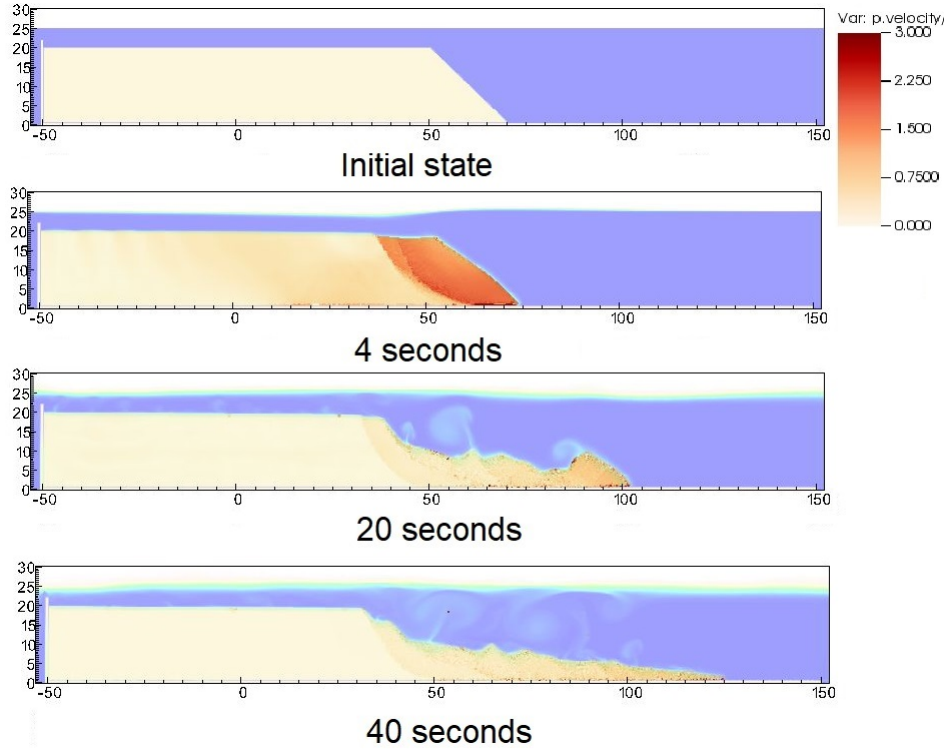


*Figure 23: Velocity during the earthquake-induced submarine landslides*

## 628      **Conclusions**

629      We have presented a numerical approach MPMICE for the simulation  
 630      of large deformation soil-fluid-structure interaction, emphasizing the simu-  
 631      lation of the earthquake-induced submarine landslides. The model uses (1)  
 632      the Material Point Method for capturing the large deformation of iso-thermal  
 633      porous media and solid structures and (2) Implicit Continuous Eulerian (com-  
 634      pressible, conservative multi-material CFD formulation) for modeling the  
 635      complex fluid flow including turbulence. This model is implemented in the  
 636      high-performance Uintah computational framework and validated against an-  
 637      alytical solution and experiment. We then demonstrate the capability of the  
 638      model to simulate the entire process of the earthquake induced submarine  
 639      landslides.

640 **Acknowledgements**

641 The authors gratefully acknowledge Dr. James Guilkey and Dr. Todd  
 642 Harman from the University of Utah for sharing the insight on the theoretical  
 643 framework of MPMICE which this work is based. This project has received  
 644 funding from the European Union's Horizon 2020 research and innovation  
 645 program under the Marie Skłodowska-Curie Actions (MSCA) Individual Fel-  
 646 lowship (Project SUBSLIDE "Submarine landslides and their impacts on  
 647 offshore infrastructures") grant agreement 101022007. The authors would  
 648 also like to acknowledge the support from the Research Council of Norway  
 649 through its Centers of Excellence funding scheme, project number 262644  
 650 Porelab. The computations were performed on High Performance Comput-  
 651 ing resources provided by UNINETT Sigma2 - the National Infrastructure  
 652 for High Performance Computing and Data Storage in Norway.

653 **Appendix: Equation derivation**

654 Before deriving the governing equation, we define the Lagrangian deriva-  
 655 tive for a state variable  $f$  as:

$$\frac{D_f f}{Dt} = \frac{\partial f}{\partial t} + \mathbf{U}_f \cdot \nabla f \quad \frac{D_s f}{Dt} = \frac{\partial f}{\partial t} + \mathbf{U}_s \cdot \nabla f \quad (101)$$

we use some definition following [16] as below:

$$-\frac{1}{V} \left[ \frac{\partial V_f}{\partial p} \right] \equiv \kappa_f \quad \text{isothermal compressibility of fluid} \quad (102)$$

$$\frac{1}{V} \left[ \frac{\partial V_f}{\partial T} \right] \equiv \alpha_f \quad \text{constant pressure thermal expansivity of fluid} \quad (103)$$

656 Then, the rate of volume with incompressible solid grains are calculated as  
 657 belows:

$$\frac{1}{V} \frac{D_f V_f}{Dt} = \frac{1}{V} \left( \left[ \frac{\partial V_f}{\partial p} \right] \frac{D_f P_{eq}}{Dt} + \left[ \frac{\partial V_f}{\partial T_f} \right] \frac{D_f T_f}{Dt} \right) = \frac{1}{V} \left( -\kappa_f \frac{D_f P_{eq}}{Dt} + \alpha_f \frac{D_f T_f}{Dt} \right) \quad (104)$$

658 *Evolution of porosity*

659 Solving the solid mass balance equation (4) with the definition of solid  
 660 mass in equation (2), it leads to the rate of porosity as belows:

$$\frac{D_s m_s}{Dt} = \frac{D_s (\phi_s \rho_s V)}{Dt} = \rho_s V \frac{D_s \phi_s}{Dt} + \phi_s V \frac{D_s \rho_s}{Dt} + \phi_s \rho_s \frac{D_s V}{Dt} = 0 \quad (105)$$

<sup>661</sup> The soil grains are assumed to be incompressible, therefore, term 2 in the  
<sup>662</sup> right hand side is zero. leading to:

$$V \frac{D_s \phi_s}{Dt} + \phi_s \frac{D_s V}{Dt} = 0 \quad (106)$$

<sup>663</sup> Dividing all terms with  $V$  with the equation  $\frac{1}{V} \frac{D_s V}{Dt} = \nabla \cdot \mathbf{U}_s$ , it leads to:

$$\frac{D_s n}{Dt} = \frac{\partial n}{\partial t} + \mathbf{U}_s \cdot \nabla n = \phi_s \nabla \cdot \mathbf{U}_s \quad (107)$$

<sup>664</sup> *Momentum conservation*

<sup>665</sup> The linear momentum balance equations for the fluid phases based on  
<sup>666</sup> mixture theory are:

$$\frac{1}{V} \frac{D_f(m_f \mathbf{U}_f)}{Dt} = \nabla \cdot (-\phi_f p_f \mathbf{I}) + \nabla \cdot \boldsymbol{\tau}_f + \bar{\rho}_f \mathbf{b} + \sum \mathbf{f}_d + \mathbf{f}_b \quad (108)$$

<sup>668</sup> On the right hand sand, the first term is the divergence of partial fluid phase  
<sup>669</sup> stress, the third term is the body force, the fourth term is the drag force  
<sup>670</sup> (momentum exchange) and the fifth term is the buoyant force described in  
<sup>671</sup> [29] for the immiscible mixtures. The buoyant force is in the form as belows:

$$\mathbf{f}_b = \boldsymbol{\sigma}_f \nabla(n) \quad (109)$$

<sup>672</sup> As a result, the linear momentum balance equations for the fluid phases  
<sup>673</sup> become as:

$$\frac{1}{V} \frac{D_f(m_f \mathbf{U}_f)}{Dt} = \frac{1}{V} \left[ \frac{\partial(m_f \mathbf{U}_f)}{\partial t} + \nabla \cdot (m_f \mathbf{U}_f \mathbf{U}_f) \right] = -\phi_f \nabla p_f + \nabla \cdot \boldsymbol{\tau}_f + \bar{\rho}_f \mathbf{b} + \sum \mathbf{f}_d \quad (110)$$

<sup>674</sup> The Reynolds stress component can be included in the term  $\boldsymbol{\tau}_f$  to consider the  
<sup>675</sup> turbulent effects if needed. To derive the linear momentum balance equation  
<sup>676</sup> for the solid phase, we begin with the linear momentum balance equation for  
<sup>677</sup> the mixture as:

$$\frac{1}{V} \frac{D_f(m_f \mathbf{U}_f)}{Dt} + \frac{1}{V} \frac{D_s(m_s \mathbf{U}_s)}{Dt} = \nabla \cdot (\boldsymbol{\sigma}) + \bar{\rho}_f \mathbf{b} + \bar{\rho}_s \mathbf{b} \quad (111)$$

<sup>678</sup> Combining Terzaghi's equation (3) and subtracting both sides with equation  
<sup>679</sup> (110), we obtain the linear momentum balance equations for the solid phase  
<sup>680</sup> as:

$$\frac{1}{V} \frac{D_s(m_s \mathbf{U}_s)}{Dt} = \nabla \cdot (\boldsymbol{\sigma}') - \phi_s \nabla p_f + \bar{\rho}_s \mathbf{b} - \sum \mathbf{f}_d + \sum \mathbf{f}_{fric} \quad (112)$$

<sup>681</sup> Here the  $\mathbf{f}_{fric}$  stems from the soil-structure interaction following the contact  
<sup>682</sup> law between the soil/structure interfaces.

683 *Energy conservation*

684 We adopt the general form of the total energy balance equation for the  
 685 porous media from [30], the total energy balance equations for the fluid phases  
 686 are:

$$\frac{1}{V} \frac{D_f(m_f(e_f + 0.5\mathbf{U}_f^2))}{Dt} = \nabla \cdot (-np_f \mathbf{I}) \cdot \mathbf{U}_f + \nabla \cdot \mathbf{q}_f + (\bar{\rho}_f \mathbf{b}) \cdot \mathbf{U}_f + \sum \mathbf{f}_d \cdot \mathbf{U}_f + \sum q_{sf} \quad (113)$$

687 Applying the product rule  $D(m\mathbf{U}^2) = D(m\mathbf{U} \cdot \mathbf{U}) = 2\mathbf{U} \cdot D(m\mathbf{U})$ , the left  
 688 hand side of equation (113) becomes:

689

$$\frac{1}{V} \frac{D_f(m_f(e_f + 0.5\mathbf{U}_f^2))}{Dt} = \frac{1}{V} \frac{D_f(m_f e_f)}{Dt} + \frac{1}{V} \frac{D_f(m_f \mathbf{U}_f)}{Dt} \cdot \mathbf{U}_f \quad (114)$$

690 Combining equations (110), (113), (114), we obtain the final form of the  
 691 internal energy balance equation for the fluid phases as:

$$\frac{1}{V} \frac{D_f(m_f e_f)}{Dt} = \frac{1}{V} \left[ \frac{\partial(m_f e_f)}{\partial t} + \nabla \cdot (m_f e_f \mathbf{U}_f) \right] = \bar{\rho}_f p_f \frac{D_f v_f}{Dt} + \nabla \cdot \mathbf{q}_f + \sum q_{sf} \quad (115)$$

692 On the right hand side, the terms include the average pressure-volume work,  
 693 the average viscous dissipation, the thermal transport and the energy ex-  
 694 change between solid and fluid respectively. The heat flux is  $\mathbf{q}_f = \bar{\rho}_f \beta_f \nabla T_f$   
 695 with  $\beta_f$  being the thermal conductivity coefficient. To derive the internal  
 696 energy balance equation for the solid phase, we introduce the rate of the  
 697 internal energy for the thermoelastic materials as a function of elastic strain  
 698 tensor  $\boldsymbol{\epsilon}_s^e$  and temperature  $T_s$  as belows:

$$\frac{m_s}{V} \frac{D_s(e_s)}{Dt} = \boldsymbol{\sigma}' : \frac{D_s(\boldsymbol{\epsilon}_s^e)}{Dt} + \frac{D_s(e_s)}{D_s(T_s)} \frac{D_s(T_s)}{Dt} = \boldsymbol{\sigma}' : \frac{D_s(\boldsymbol{\epsilon}_s^e)}{Dt} + c_v \frac{D_s(T_s)}{Dt} \quad (116)$$

699  $c_v$  is the specific heat at the constant volume of the solid materials. The total  
 700 energy balance equation for the mixture based on [30] can be written as:

701

$$\begin{aligned} \frac{1}{V} \frac{D_f(m_f(e_f + 0.5\mathbf{U}_f^2))}{Dt} + \frac{1}{V} \frac{D_s(m_s(e_s + 0.5\mathbf{U}_s^2))}{Dt} &= \nabla \cdot (-\phi_f p_f \mathbf{I}) \cdot \mathbf{U}_f \\ &+ \nabla \cdot (\boldsymbol{\sigma}' - \phi_s p_f \mathbf{I}) \cdot \mathbf{U}_s + (-\phi_f p_f \mathbf{I}) : \nabla \mathbf{U}_f + \boldsymbol{\sigma}' : \nabla \mathbf{U}_s \\ &+ (\bar{\rho}_f \mathbf{b}) \cdot \mathbf{U}_f + (\bar{\rho}_s \mathbf{b}) \cdot \mathbf{U}_s + \nabla \cdot \mathbf{q}_f + \nabla \cdot \mathbf{q}_s + \sum \mathbf{f}_d \cdot (\mathbf{U}_f - \mathbf{U}_s) \end{aligned} \quad (117)$$

702 Subtracting equation (117), (116) to equations (113) and (112), we obtained  
 703 the internal energy balance equation for solid phase as:

$$\boldsymbol{\sigma}' : \frac{D_s(\epsilon_s^e)}{Dt} + \frac{m_s}{V} c_v \frac{D_s(T_s)}{Dt} = \Delta W_s + \Delta W_{friction} + \nabla \cdot \mathbf{q}_s - \sum q_{sf} \quad (118)$$

704 On the right hand side, the terms include the work rate from frictional sliding  
 705 between solid materials  $\Delta W_{friction}$ , thermal transport and energy exchange  
 706 between solid and fluid respectively. The heat flux is  $\mathbf{q}_s = \bar{\rho}_s \beta_s \nabla T_s$  with  $\beta_s$   
 707 being the thermal conductivity of the solid materials, the mechanical work  
 708 rate  $\Delta W_s = \boldsymbol{\sigma}' : \frac{D_s(\epsilon_s^e)}{Dt} = \boldsymbol{\sigma}' : (\frac{D_s(\epsilon_s^e)}{Dt} + \frac{D_s(\epsilon_s^p)}{Dt})$  computed from the constitutive  
 709 model with  $\epsilon_s^p$  is the plastic strain tensor, . By subtracting the term  $\boldsymbol{\sigma}' : \frac{D_s(\epsilon_s^e)}{Dt}$ ,  
 710 we get the final form of the energy balance equation as:

$$\frac{m_s}{V} c_v \frac{D_s(T_s)}{Dt} = \boldsymbol{\sigma}' : \frac{D_s(\epsilon_s^p)}{Dt} + \Delta W_{friction} + \nabla \cdot \mathbf{q}_s - \sum q_{sf} \quad (119)$$

### 711 Advanced Fluid Pressure

712 The discretization of the pressure equation begins with the Lagrangian  
 713 cell face velocity and the equation for the pressure as:

$$\bar{\rho}_{f,FC} \frac{\mathbf{U}_{f,FC}^{n+1} - \mathbf{U}_{f,FC}^n}{dt} = n \nabla^{FC} P_{f,c}^{n+1} + \bar{\rho}_{f,FC} \mathbf{b} \quad (120)$$

714

$$\kappa \frac{dP}{dt} = \nabla^c \cdot \mathbf{U}_{f,FC}^{n+1} \quad (121)$$

715 The divergence of the equation (120) with  $\nabla \cdot \mathbf{b} = 0$  is:

$$\nabla^c \cdot \mathbf{U}_{f,FC}^{n+1} - \nabla^c \cdot \mathbf{U}_{f,FC}^n = \nabla^c \frac{\Delta t}{\rho_{f,FC}^n} \cdot \nabla^{FC} (P_{f,c}^n + \Delta P_{f,c}^n) \quad (122)$$

716 To solve this equation, we define the cell face intermediate velocity  $\mathbf{U}_{f,FC}^*$  as:

$$\bar{\rho}_{f,FC} \frac{\mathbf{U}_{f,FC}^* - \mathbf{U}_{f,FC}^n}{\Delta t} = n \nabla^{FC} P_{f,c}^n + \bar{\rho}_{f,FC} \mathbf{b} \quad (123)$$

717 The divergence of the equation (123) is:

$$\nabla^c \cdot \mathbf{U}_{f,FC}^* - \nabla^c \cdot \mathbf{U}_{f,FC}^n = \nabla^c \frac{\Delta t}{\rho_{f,FC}^n} \cdot \nabla^{FC} P_{f,c}^n \quad (124)$$

<sup>718</sup> Combining equations (121, 122, 124), it leads to:

$$\left( \kappa - \nabla^c \frac{\Delta t}{\rho_{f,FC}^n} \cdot \nabla^{FC} \right) \Delta P_{fc}^n = -\nabla^c \cdot \mathbf{U}_{f,FC}^* \quad (125)$$

<sup>719</sup> When the fluid is incompressible,  $\kappa$  approaches to zero and the equation  
<sup>720</sup> (125) becomes the Poisson's equation for the incompressible fluid flow.

### <sup>721</sup> Momentum and Energy exchange with an implicit solver

<sup>722</sup> Considering the fluid momentum balance equation as:

$$(m\mathbf{U})_{f,FC}^{n+1} = (m\mathbf{U})_{f,FC}^n - \Delta t(Vn\nabla^{FC}P_{fc}^n + m_f\mathbf{b}) + VK\Delta t(\mathbf{U}_{s,FC}^{n+1} - \mathbf{U}_{f,FC}^{n+1}) \quad (126)$$

<sup>723</sup> And assuming  $m_{f,FC}^{n+1} = m_{f,FC}^n$ , we get:

$$\mathbf{U}_{f,FC}^{n+1} = \mathbf{U}_{f,FC}^n - \Delta t\left(\frac{\nabla^{FC}P_{fc}^n}{\rho_{f,FC}^n} + \mathbf{b}\right) + \frac{\Delta tK}{\bar{\rho}_{f,FC}^n}(\mathbf{U}_{s,FC}^{n+1} - \mathbf{U}_{f,FC}^{n+1}) \quad (127)$$

<sup>724</sup> As defined in the section 'Advanced Fluid Pressure', the cell face intermediate  
<sup>725</sup> fluid velocity  $\mathbf{U}_{f,FC}^* = \Delta t(\nabla^{FC}P_{fc}^n/\rho_{f,FC}^n + \mathbf{b})$  is computed as:

$$\mathbf{U}_{f,FC}^{n+1} = \mathbf{U}_{f,FC}^* + \frac{\Delta tK}{\bar{\rho}_{f,FC}^n}(\mathbf{U}_{s,FC}^{n+1} - \mathbf{U}_{f,FC}^{n+1}) \quad (128)$$

<sup>726</sup> Considering the solid momentum balance equation as:

$$(m\mathbf{U})_{s,FC}^{n+1} = (m\mathbf{U})_{s,FC}^n - \Delta t(V\nabla^{FC} \cdot \boldsymbol{\sigma}'^n - V(1-n)\nabla^{FC}P_{fc}^n + m_s\mathbf{b}) - VK\Delta t(\mathbf{U}_{s,FC}^{n+1} - \mathbf{U}_{f,FC}^{n+1}) \quad (129)$$

<sup>727</sup> We define the cell face intermediate solid velocity as  $\mathbf{U}_{s,FC}^* = \Delta t(\nabla^{FC} \cdot \boldsymbol{\sigma}'^n / \bar{\rho}_{s,FC}^n - \nabla^{FC}P_{fc}^n / \rho_s + \mathbf{b})$  leading to:

$$\mathbf{U}_{s,FC}^{n+1} = \mathbf{U}_{s,FC}^* - \frac{\Delta tK}{\bar{\rho}_{s,FC}^n}(\mathbf{U}_{s,FC}^{n+1} - \mathbf{U}_{f,FC}^{n+1}) \quad (130)$$

<sup>729</sup> Combining equation (128) and (130) we get:

$$\begin{aligned} \mathbf{U}_{f,FC}^* + \Delta\mathbf{U}_{f,FC} &= \mathbf{U}_{f,FC}^* + \frac{\Delta tK}{\bar{\rho}_{f,FC}^n}(\mathbf{U}_{s,FC}^* + \Delta\mathbf{U}_{s,FC} - \mathbf{U}_{f,FC}^* - \Delta\mathbf{U}_{f,FC}) \\ \mathbf{U}_{s,FC}^* + \Delta\mathbf{U}_{s,FC} &= \mathbf{U}_{s,FC}^* - \frac{\Delta tK}{\bar{\rho}_{s,FC}^n}(\mathbf{U}_{s,FC}^* + \Delta\mathbf{U}_{s,FC} - \mathbf{U}_{f,FC}^* - \Delta\mathbf{U}_{f,FC}) \end{aligned} \quad (131)$$

730 Rearranging the equation (131), it leads to the linear system of equations as  
 731 belows:

$$\begin{vmatrix} (1 + \beta_{12,FC}) & -\beta_{12,FC} \\ -\beta_{21,FC} & (1 + \beta_{21,FC}) \end{vmatrix} \begin{vmatrix} \Delta \mathbf{U}_{f,FC} \\ \Delta \mathbf{U}_{s,FC} \end{vmatrix} = \begin{vmatrix} \beta_{12,FC} (\mathbf{U}_{s,FC}^* - \mathbf{U}_{f,FC}^*) \\ \beta_{21,FC} (\mathbf{U}_{f,FC}^* - \mathbf{U}_{s,FC}^*) \end{vmatrix}$$

732 Solving this linear equations with  $\beta_{12,FC} = (\Delta t K) / \bar{\rho}_{f,FC}^n$  and  $\beta_{21,FC} =$   
 733  $(\Delta t K) / \bar{\rho}_{s,FC}^n$  with K is the momentum exchange coefficient. Similar deriva-  
 734 tion can be performed to computed the cell-center velocity increment leading  
 735 to:

$$\begin{vmatrix} (1 + \beta_{12c}) & -\beta_{12c} \\ -\beta_{21c} & (1 + \beta_{21c}) \end{vmatrix} \begin{vmatrix} \Delta \mathbf{U}_{f,c} \\ \Delta \mathbf{U}_{sc} \end{vmatrix} = \begin{vmatrix} \beta_{12c} (\mathbf{U}_{sc}^* - \mathbf{U}_{f,c}^*) \\ \beta_{21c} (\mathbf{U}_{f,c}^* - \mathbf{U}_{sc}^*) \end{vmatrix}$$

736 with  $\beta_{12c} = (\Delta t K) / \bar{\rho}_{f,c}^n$  and  $\beta_{21c} = (\Delta t K) / \bar{\rho}_{sc}^n$  and the cell-centered interme-  
 737 diate velocity can be calculated by:

$$\begin{aligned} \mathbf{U}_{f,c}^* &= \mathbf{U}_{f,c}^n + \Delta t \left( -\frac{\nabla P_{f,c}^{n+1}}{\rho_{f,c}^n} + \frac{\nabla \cdot \boldsymbol{\tau}_{f,c}^n}{\bar{\rho}_{f,c}^n} + \mathbf{b} \right) \\ \mathbf{U}_{sc}^* &= \mathbf{U}_{sc}^n + \Delta t \left( \frac{\nabla \cdot \boldsymbol{\sigma}_c'^n}{\bar{\rho}_{sc}^n} - \frac{\nabla P_{f,c}^{n+1}}{\rho_s} + \mathbf{b} \right) \end{aligned} \quad (132)$$

738 For generalize multi materials i,j = 1:N, the linear equations is in the form  
 739 as:

$$\begin{vmatrix} (1 + \beta_{ij}) & -\beta_{ij} \\ -\beta_{ji} & (1 + \beta_{ji}) \end{vmatrix} \begin{vmatrix} \Delta \mathbf{U}_i \\ \Delta \mathbf{U}_j \end{vmatrix} = \begin{vmatrix} \beta_{ij} (\mathbf{U}_i^* - \mathbf{U}_j^*) \\ \beta_{ji} (\mathbf{U}_j^* - \mathbf{U}_i^*) \end{vmatrix}$$

740 Similar approach applied for the ernergy exchange term leading to:

$$\begin{vmatrix} (1 + \eta_{ij}) & -\eta_{ij} \\ -\eta_{ji} & (1 + \eta_{ji}) \end{vmatrix} \begin{vmatrix} \Delta T_i \\ \Delta T_j \end{vmatrix} = \begin{vmatrix} \eta_{ij} (T_i^n - T_j^n) \\ \eta_{ji} (T_j^n - T_i^n) \end{vmatrix}$$

741 with  $\eta$  is the energy exchange coefficient.

## 742 References

- 743 [1] D. Yuk, S. Yim, P.-F. Liu, Numerical modeling of submarine mass-  
 744 movement generated waves using RANS model, Computers and Geo-  
 745 sciences 32 (7) (2006) 927–935. doi:10.1016/j.cageo.2005.10.028.  
 746 URL <https://doi.org/10.1016/j.cageo.2005.10.028>

- 747 [2] S. Glimsdal, J.-S. L'Heureux, C. B. Harbitz, F. Løvholt, The 29th january 2014 submarine landslide at statland, norway—landslide dynamics,  
748 tsunami generation, and run-up, *Landslides* 13 (6) (2016) 1435–1444.  
749 doi:10.1007/s10346-016-0758-7.  
750 URL <https://doi.org/10.1007/s10346-016-0758-7>
- 752 [3] S. Abadie, D. Morichon, S. Grilli, S. Glockner, Numerical simulation  
753 of waves generated by landslides using a multiple-fluid  
754 navier–stokes model, *Coastal Engineering* 57 (9) (2010) 779–794.  
755 doi:10.1016/j.coastaleng.2010.03.003.  
756 URL <https://doi.org/10.1016/j.coastaleng.2010.03.003>
- 757 [4] M. Rauter, S. Viroulet, S. S. Gylfadóttir, W. Fellin, F. Løvholt, Granular  
758 porous landslide tsunami modelling – the 2014 lake askja flank collapse,  
759 *Nature Communications* 13 (1) (Feb. 2022). doi:10.1038/s41467-022-  
760 28296-7.  
761 URL <https://doi.org/10.1038/s41467-022-28296-7>
- 762 [5] Q.-A. Tran, W. Sołowski, Generalized interpolation material point  
763 method modelling of large deformation problems including strain-  
764 rate effects – application to penetration and progressive fail-  
765 ure problems, *Computers and Geotechnics* 106 (2019) 249–265.  
766 doi:10.1016/j.compgeo.2018.10.020.  
767 URL <https://doi.org/10.1016/j.compgeo.2018.10.020>
- 768 [6] T. Capone, A. Panizzo, J. J. Monaghan, SPH modelling of water  
769 waves generated by submarine landslides, *Journal of Hydraulic Research*  
770 48 (sup1) (2010) 80–84. doi:10.1080/00221686.2010.9641248.  
771 URL <https://doi.org/10.1080/00221686.2010.9641248>
- 772 [7] X. Zhang, E. Oñate, S. A. G. Torres, J. Bleyer, K. Krabbenhoft, A  
773 unified lagrangian formulation for solid and fluid dynamics and its pos-  
774 sibility for modelling submarine landslides and their consequences, *Com-  
775 puter Methods in Applied Mechanics and Engineering* 343 (2019) 314–  
776 338. doi:10.1016/j.cma.2018.07.043.  
777 URL <https://doi.org/10.1016/j.cma.2018.07.043>
- 778 [8] R. Dey, B. C. Hawlader, R. Phillips, K. Soga, Numerical modelling  
779 of submarine landslides with sensitive clay layers, *Géotechnique* 66 (6)

- (2016) 454–468. doi:10.1680/jgeot.15.p.111.  
URL <https://doi.org/10.1680/jgeot.15.p.111>

[9] S. Bandara, K. Soga, Coupling of soil deformation and pore fluid flow using material point method, *Computers and Geotechnics* 63 (2015) 199–214. doi:10.1016/j.compgeo.2014.09.009.  
URL <https://doi.org/10.1016/j.compgeo.2014.09.009>

[10] A. P. Tampubolon, T. Gast, G. Klár, C. Fu, J. Teran, C. Jiang, K. Museth, Multi-species simulation of porous sand and water mixtures, *ACM Transactions on Graphics* 36 (4) (2017) 1–11. doi:10.1145/3072959.3073651.  
URL <https://doi.org/10.1145/3072959.3073651>

[11] A. S. Baumgarten, K. Kamrin, A general constitutive model for dense, fine-particle suspensions validated in many geometries, *Proceedings of the National Academy of Sciences* 116 (42) (2019) 20828–20836. doi:10.1073/pnas.1908065116.  
URL <https://doi.org/10.1073/pnas.1908065116>

[12] Q.-A. Tran, W. Sołowski, Temporal and null-space filter for the material point method, *International Journal for Numerical Methods in Engineering* 120 (3) (2019) 328–360. doi:10.1002/nme.6138.  
URL <https://doi.org/10.1002/nme.6138>

[13] X. Zheng, F. Pisanò, P. J. Vardon, M. A. Hicks, An explicit stabilised material point method for coupled hydromechanical problems in two-phase porous media, *Computers and Geotechnics* 135 (2021) 104112. doi:10.1016/j.compgeo.2021.104112.  
URL <https://doi.org/10.1016/j.compgeo.2021.104112>

[14] Q. A. Tran, W. Sołowski, M. Berzins, J. Guilkey, A convected particle least square interpolation material point method, *International Journal for Numerical Methods in Engineering* 121 (6) (2019) 1068–1100. doi:10.1002/nme.6257.  
URL <https://doi.org/10.1002/nme.6257>

[15] J.-S. Chen, M. Hillman, S.-W. Chi, Meshfree methods: Progress made after 20 years, *Journal of Engineering Mechanics* 143 (4) (Apr. 2017).

- 812 doi:10.1061/(asce)em.1943-7889.0001176.  
813 URL [https://doi.org/10.1061/\(asce\)em.1943-7889.0001176](https://doi.org/10.1061/(asce)em.1943-7889.0001176)
- 814 [16] B. A. Kashiwa, A multifield model and method for fluid-structure in-  
815 teraction dynamics, Tech. Rep. LA-UR-01-1136, Los Alamos National  
816 Laboratory (2001).
- 817 [17] J. Guilkey, T. Harman, B. Banerjee, An eulerian-lagrangian  
818 approach for simulating explosions of energetic devices,  
819 Computers and Structures 85 (11) (2007) 660 – 674.  
820 doi:<https://doi.org/10.1016/j.compstruc.2007.01.031>.  
821 URL <http://www.sciencedirect.com/science/article/pii/S0045794907000429>
- 822 [18] A. S. Baumgarten, B. L. Couchman, K. Kamrin, A coupled finite volume  
823 and material point method for two-phase simulation of liquid-sediment  
824 and gas-sediment flows, Computer Methods in Applied Mechanics and  
825 Engineering 384 (2021) 113940. doi:10.1016/j.cma.2021.113940.  
826 URL <https://doi.org/10.1016/j.cma.2021.113940>
- 827 [19] S. Bardenhagen, J. Guilkey, K. Roessig, J. Brackbill, W. Witzel,  
828 J.C.Foster, An improved contact algorithm for the material point  
829 method and application to stress propagation in granular material,  
830 CMES-Computer Modeling in Engineering and Sciences 2 (2001) 509–  
831 522. doi:10.3970/cmes.2001.002.509.
- 832 [20] J. A. M. K. R. Beetstra, M. A. van der Hoef, Drag force of intermediate  
833 reynolds number flow past mono- and bidisperse arrays of spheres,  
834 Fluid Mechanics and Transport Phenomena 53 (2) (2007) 489 – 501.  
835 doi:<https://doi.org/10.1002/aic.11065>.
- 836 [21] R. W. Stewart, The air-sea momentum exchange, Boundary-Layer Me-  
837 teorology 6 (1-2) (1974) 151–167. doi:10.1007/bf00232481.  
838 URL <https://doi.org/10.1007/bf00232481>
- 839 [22] S. G. Bardenhagen, E. M. Kober, The generalized interpolation material  
840 point method, Computer Modeling in Engineering and Sciences 5 (2004)  
841 477–496. doi:10.1016/j.compgeo.2021.104199.  
842 URL <https://doi.org/10.3970/cmes.2004.005.477>
- 843 [23] S. G. Amiri, E. Taheri, A. Lavasan, A hybrid finite element model for  
844 non-isothermal two-phase flow in deformable porous media, Computers

- 845 and Geotechnics 135 (2021) 104199. doi:10.1016/j.compgeo.2021.104199.  
846 URL <https://doi.org/10.1016/j.compgeo.2021.104199>
- 847 [24] S. A. R. C. Mariotti;, P. Heinrich, Numerical simulation of sub-  
848 marine landslides and their hydraulic effects, Journal of Waterway, Port,  
849 Coastal, and Ocean Engineering 123 (4) (1997).  
850 doi:[https://doi.org/10.1061/\(ASCE\)0733-950X\(1997\)123:4\(149\)](https://doi.org/10.1061/(ASCE)0733-950X(1997)123:4(149)).
- 851 [25] A. Alsardi, A. Yerro, Runout Modeling of Earthquake-Triggered  
852 Landslides with the Material Point Method, pp. 21–31.  
853 arXiv:<https://ascelibrary.org/doi/pdf/10.1061/9780784483428.003>,  
854 doi:10.1061/9780784483428.003.  
855 URL <https://ascelibrary.org/doi/abs/10.1061/9780784483428.003>
- 856 [26] H. N., O. A., B. H. H., R. P., R. Fukagawa, Seismic slope failuremod-  
857 ellng using the mesh-free sph method, International Journal of Geomate  
858 (2013) 660–665.
- 859 [27] T. Bhandari, F. Hamad, C. Moormann, K. Sharma,  
860 B. Westrich, Numerical modelling of seismic slope failure us-  
861 ing mpm, Computers and Geotechnics 75 (2016) 126–134.  
862 doi:<https://doi.org/10.1016/j.compgeo.2016.01.017>.  
863 URL <https://www.sciencedirect.com/science/article/pii/S0266352X16000264>
- 864 [28] D. Muir Wood, Soil behaviour and critical state soil mechanics, Cam-  
865 bridge University Press, United Kingdom, 1990.
- 866 [29] D. Drumheller, On theories for reacting immiscible mixtures, Interna-  
867 tional Journal of Engineering Science 38 (3) (2000) 347 – 382.  
868 doi:[https://doi.org/10.1016/S0020-7225\(99\)00047-6](https://doi.org/10.1016/S0020-7225(99)00047-6).  
869 URL <http://www.sciencedirect.com/science/article/pii/S0020722599000476>
- 870 [30] S. Hassanzadeh, Derivation of basic equations of mass transport in  
871 porous media, part1: Macroscopic balance laws, Advances in Wa-  
872 ter Resources 9 (1986) 196–206. doi:[https://doi.org/10.1016/0309-1708\(86\)90024-2](https://doi.org/10.1016/0309-1708(86)90024-2).